NTNU – Trondheim
Norwegian University of
Science and Technology

Quantitative Comparison of PET/MR and PET/CT for Imaging of Lymphoma Patients

Silje Kjærnes Olsen

Master of Science in Physics and Mathematics
Submission date: June 2015
Supervisor: Pål Erik Goa, IFY
Co-supervisor: Live Eikenes, ISB

Norwegian University of Science and Technology
Department of Physics

Abstract

Positron emission tomography/computed tomography (PET/CT), a multimodality imaging tool, is today the golden standard in diagnosis, staging and response monitoring of lymphoma patients, while it is investigated if positron emission tomography/magnetic resonance (PET/MR) is superior to PET/CT and should be the gold standard in imaging of lymphoma patients in the future.

In this study, PET/MR and PET/CT have been quantitatively compared for imaging of lymphoma patients, by the semi-quantitative measure standardized uptake value (SUV) from the PET images and the apparent diffusion coefficient (ADC) from diffusion-weighted MR images. The correlation between SUV from PET/MR and PET/CT and between SUV and ADC was evaluated, as well as the PET image quality, measured by the coefficient of variance (COV).

Fourteen lymphoma patients were included, and underwent a PET/CT examination followed by a PET/MR examination. Regions of interest (ROIs) were made in the same forty-two lesions in the PET images of PET/MR and PET/CT for the SUV analysis. Seven lesions were included in the ADC analysis, where six different shaped ROIs were drawn in each lesion, to see if the shape influenced the result. COV was measured in ROIs in the liver of each patient in the PET images.

A strong correlation was found between SUV from PET/MR and PET/CT, and the difference in SUV was not statistically significantly. No correlation was found between ADC and SUV, in any of the different shaped ROIs for ADC measurements. COV was significantly increased in PET/MR, compared to PET/CT, indicating a reduced PET image quality for PET/MR. The SUV measurements from PET/MR are similar to those from PET/CT, hence the two modalities are quantitatively comparable. Qualitative studies must also be performed to determine if PET/MR is superior to PET/CT for imaging of lymphoma patients. More lesions should be included in the ADC analysis, to evaluate the relationship between SUV and ADC. Further work should be performed to find the cause of the reduced image quality of PET images obtained from PET/MR.

Sammendrag

Avbildningsmodaliteten positronemisjonstomografi/computertomografi (PET/CT) er i dag 'gullstandarden' for å diagnostisere, undersøke utbredelsen av metastaser og vurdere terapirespons for lymfekreftpasienter. Det gjøres forskning på PET/magnetisk resonanstomografi (PET/MR) for å vurdere om denne avbildningsmodaliteten er overlegen PET/CT og bør være den nye 'gullstandarden' for avbildning av lymfekreftpasienter i fremtiden.

PET/MR og PET/CT har blitt sammenlignet ved avbildning av lymfekreftpasienter i dette studiet, ved hjelp av det semi-kvantitative målet standarisert opptaksverdi (SUV), målt i PET-bildene, og den kvantitative tilsynelatende diffusjonskoeffisienten (ADC) fra diffusjonsvektede MR bilder. Korrelasjonen mellom SUV fra PET/MR og PET/CT, og mellom SUV og ADC, har blitt undersøkt. I tillegg har bildekvaliteten av PET-bildene blitt målt, ved hjelp av varianskoeffisienten (COV).

Fjorten lymfompasienter ble inkludert i studien, hvor en PET/CT undersøkelse ble etterfulgt av en PET/MR undersøkelse. Regioner av interesse (ROIer) ble laget i de samme førtito lesjonene i PET-bildene fra PET/MR og PET/CT, som ble brukt i SUV-analysen. Syv lesjoner ble inkludert i ADC-analysen, hvor ROIer med seks ulike former ble tegnet i hver lesjon, for å se om formen på ROIene hadde innvirkning på resultatet. COV ble målt i PET-bildene, i ROIer som var plassert i leveren på hver pasient.

Det ble funnet en sterk korrelasjon mellom SUV fra PET/MR og PET/CT, og forskjellen i SUV var ikke statistisk signifikant. Det ble ikke funnet korrelasjon mellom ADC og SUV i noen av de seks forskjellig formede ROIene hvor ADC ble målt. COV var signifikant høyere for PET/MR i forhold til PET/CT, noe som indikerer at bildekvaliten er redusert i PET-bildene fra PET/MR.

PET/MR og PET/CT er kvantitativt sammenlignbare, ettersom at SUV er tilsvarende for PET/MR som for PET/CT. For å vurdere om PET/MR bør erstatte PET/CT i avbildning av lymfekreftpasienter, må også kvalitative sammenligninger gjennomføres. For å finne en sammenheng mellom SUV og ADC må flere lesjoner inkluderes i ADC-analysen. Flere studier bør gjennomføres for å finne årsaken til den reduserte bildekvaliteten i PET-bildene fra PET/MR.

Acknowledgements

I would like to express my very great appreciation to my main supervisor, Associated Professor Live Eikenes (Norwegian University of Science and Technology (NTNU), Trondheim, Norway), who gave me great support and a lot of valuable feedback during the work with my thesis.

I would also like to offer a special thank to Medical Physicist Anna Karlberg (St. Olavs Hospital, Trondheim, Norway), who gladly answered all of my numerous technical questions.

Advices and feedback on my thesis from my supervisor at the Department of Physics, Associated Professor Pål Erik Goa, was also of great value, and thanks to Nuclear Medicine Physician Thomas Keil (St. Olavs Hospital, Trondheim, Norway) for providing me knowledge about lymphoma and nuclear medicine. The radiographers at St. Olavs Hospital are also deserving gratitude for their assist and patience.

I would also like to thank two of my fellow students, Johanna and Vera, for sharing knowledge, experience and motivation, and my fiancé, Endre, for his great support.

Silje Kjærnes Olsen
June 2015

Contents

Abstract **I**

Sammendrag **II**

Acknowledgements **III**

Contents **IV**

Acronyms **VI**

I Introduction **1**

1 Motivation and objective 1

2 Theory 3

2.1 Lymphoma 3

2.2 PET 5

2.2.1 Attenuation correction and scatter correction . 7

2.2.2 The PET detector 8

2.2.3 PET tracers 10

2.2.4 Semi-quantitative measurement in PET: Standardized uptake value 10

2.2.5 COV 12

2.3 MR 12

2.3.1 Gradients 13

2.3.2 MR sequences 15

2.3.3 Diffusion weighted imaging and apparent diffusion coefficient - a MR quantitative measurement 18

2.4 CT 19

2.5 PET/CT 20

2.5.1 Attenuation correction 20

2.6 PET/MR 21

2.6.1 Attenuation correction 21

2.6.2 Detectors 22

2.7 Lymphoma staging 24

II Materials and methods **26**
1 Subjects . . . 26
2 Image acquisition . . . 27
2.1 PET/CT . . . 27
2.2 PET/MR . . . 28
3 Image analysis . . . 29
3.1 SUV . . . 29
3.2 ADC . . . 30
3.3 COV . . . 31
4 Statistics . . . 31

III Results **32**
1 SUV_{MR} and SUV_{CT} . . . 32
2 SUV_{MR} versus SUV_{CT} . . . 35
3 ADC . . . 38
3.1 ADCmin and ADCmean . . . 38
3.2 ADC versus SUV . . . 40
4 COV . . . 40

IV Discussion **41**
1 SUV_{MR} and SUV_{CT} . . . 41
2 SUV_{MR} versus SUV_{CT} . . . 41
3 ADC . . . 43
4 COV . . . 45

V Conclusion **47**

References **48**

Appendices **58**

A ADC versus SUV **59**

Acronyms

^{18}F-FDG	^{18}F-2-deoxy-D-glucose
1D	one-dimensional
2D	two-dimensional
ADC	analog-to-digital converter
ADC	apparent diffusion coefficient
APD	avalanche photodiodes
COV	coefficient of variance
DLBCL	diffuse large B-cell lymphoma
DWI	diffusion weighted imaging
EANM	European Association of Nuclear Medicine
FBP	filtered-backprojection
FID	free induction decay
FL	follicular lymphoma
FOV	field of view
FWHM	Full-Width Half-Maximum
HL	Hodgkin lymphoma
HU	Hounsfield units
LAC	linear attenuation coefficient
LOR	line-of-response
MR	magnetic resonance

NHL	non-Hodgkin lymphoma
NSCLC	non-small cell lung cancer
OSEM	ordered subset expectation maximization
PET/CT	positron emission tomography/computed tomography
PET/MR	positron emission tomography/magnetic resonance
PFS	progression-free survival
PMTs	photomultiplier tubes
PSF	point spread function
RF	radio frequency
ROI	region-of-interest
SiPM	silicon photomultipliers
SNR	signal-to-noise ratio
SUV	standardized uptake value
TOF	time-of-flight
UTE	ultrashort echo time

Chapter I

Introduction

1 Motivation and objective

Positron emission tomography/computed tomography (PET/CT) is a well established multimodality imaging tool in the clinic, which is used for diagnosis, staging and therapy monitoring in oncology [59]. The multimodality provides both functional/metabolic and anatomical imaging, by PET and CT, respectively. PET is widely used in oncology as tumors have an increased metabolism, which gives an increased intensity in the images, while CT is used for imaging of injuries, tumors and other conditions, and is excellent for bone imaging.

Magnetic resonance (MR) imaging is also an anatomic image modality which has a superior soft tissue contrast, and especially superior for brain imaging, compared to CT. PET and MR have therefore also been combined to investigate if PET/MR could be superior to PET/CT for some patient groups, especially in patient groups or parts of the body where MR is superior to CT [59]. MR can also provide functional information such as perfusion and diffusion, which is complementary to the information obtained from PET, and MR spectroscopy can be used to find metabolites [18].

Another advantage of integrated simultaneous PET/MR systems is that the PET and MR images can be acquired simultaneously, which means that motion correction can be done in real-time using the anatomic MR data. This is in contrast to PET/CT where the PET and CT scan are performed sequentially because the radiation from CT will affect the PET acquisition.

Furthermore, the radiation exposure is reduced when utilizing MR instead of CT. In the current study lymphoma patients are included, which may be younger people who will undergo repeated PET scans during therapy. It is therefore important to reduce the total radiation dose, and in a study including children with multifocal malignant diseases, the radiation exposure was reduced by around 80% for PET/MR examinations compared to PET/CT examinations [28].

Staging by the use of PET has some limitations, and can cause false positive and false negative diagnosis [53]. The most used tracer in PET, ^{18}F-2-deoxy-D-glucose (^{18}F-FDG), which is not tumor-specific, also accumulate in inflammations and non-malignant tissue as the brain, heart and kidneys [31]. In addition, some lymphoma subtypes are not FDG avid (low uptake of FDG) [53], and PET/MR might be a better alternative than PET/CT in these cases, as the excellent soft tissue contrast of anatomic MR images and diffusion-weighted images can be used in the diagnosis.

Although MR has a lot of advantages compared to CT, and the combination of PET/MR has shown promising results [43][28], PET/MR is not as well established as PET/CT due to several technical challenges. One of the main challenges is the attenuation correction of the PET images, which is much more challenging when based on MR images compared to CT images. The quality of the PET images is highly dependent on the attenuation correction.

A PET/MR examination is also more time consuming than a PET/CT examination (about one hour against 20-30 minutes, respectively), which may be uncomfortable for the patient, increasing the probability of patient motion (causing imaging artifacts) and lowering the throughput of patients.

Further work must be done to determine the application areas of PET/MR, and if PET/MR is inferior, superior, equal or complementary to PET/CT for diagnosis, staging and response monitoring in different patient groups. This work will be time consuming as all patient groups which are now referred to PET/CT, must be included and undergo PET/MR examinations.

Both quantitative and qualitative comparisons of the two modalities are required, however, this study will focus on quantitative measurements. Standardized uptake value (SUV) is a semi-quantitative measure of glucose metabolism measured from PET images, which is increased in cancer cells and often used for quantification of malignancy. Cancer is also characterized by increased cellularity, which is found to be inversely correlated to apparent diffusion coefficient (ADC) [63], a quantitative measure of random microscopic motion of water molecules, obtained from diffusion-weighted MR imaging. As cancer is characterized by both increased glucose metabolism and increased cellularity, both SUV and ADC should be able to quantify malignancy, and have been used clinically for evaluating tumor aggressiveness and treatment response. The introduction of PET/MR offers the ability to combine the information from SUV and ADC measurements, and it is therefore wanted to know if either of them is preferred or if they provide similar or complementary information. If ADC can be used to quantify therapy response, the radiation exposure for the patient can be greatly reduced by replacing the repeated PET examinations with MR examinations, as the radiation dose of FDG for instance is approximately 6 mSv for a injected dose of 300 MBq [7]. The relationship between ADC and SUV is not yet identified [16], and varying results have been found regarding

the correlation between ADC and SUV in lymphoma patients. Some studies did not find a correlation [16] [63], while others found an inverse significant correlation between ADC and SUV [62] [64].

SUV is often used in diagnosis, staging and therapy monitoring of cancer patients, in combination with visual evaluation of PET images. The first aim of this study was to compare SUV in lymphoma patients measured from PET/MR and PET/CT, to evaluate if SUV is equivalent for PET/MR and the golden standard in imaging of lymphoma patients, PET/CT. The second aim was to investigate if SUV and ADC correlate, as it is wanted to know if there is a relation between them.

If PET images from PET/MR can give the same information and are of the same quality as from PET/CT, PET/MR can be used for imaging of lymphoma patients. The last aim was therefore to evaluate the image quality of the PET images, in terms of the coefficient of variance (COV), to see if the image quality is as good for PET/MR as for PET/CT.

2 Theory

2.1 Lymphoma

Lymphoma is a tumor of lymphoid tissue which is usually malignant [49] and the most common blood cancer [2]. The lymphatic system consists of lymph (a fluid), lymph nodes, lymph vessels, the tonsils, the spleen, the thymus gland, and Peyer's patches in the intestine (Figure 2.1). The functions of the system is to control body fluids, to transport fats from the digestive tract to the blood, to destroy harmful microorganisms and to produce lymphocytes.

Lymphoid tissue consists primarily of lymphocytes, a type of white blood cells, and lymphomas are caused by genetic changes within one lymphocyte, which cause an accumulation of cells [25]. There exist different types of lymphoma, probably because of genetic changes at different stages of the life cycle of the lymphocytes.

Lymphomas are broadly divided into Hodgkin lymphoma (HL) and non-Hodgkin lymphoma (NHL) according to biopsy. The two main subtypes develop and spread differently, and hence have different treatments [2]. Tumors with Reed-Sternberg cells are classified as HL [42], which often affects younger adults (15 to 35 years) and older adults (over age 50), and consist of six subtypes [1]. HL usually starts in lymph nodes and often spread to other lymph nodes, however, it may also spread to other organs.

NHL is more common than HL, and the incidence is in total increasing with age and is rare among children [30]. NHL is divided into two large groups, B-cell and T-cell lymphoma (originating from an abnormal B-lymphocytes or T-lymphocytes, respectively), and is also described as aggressive or indolent

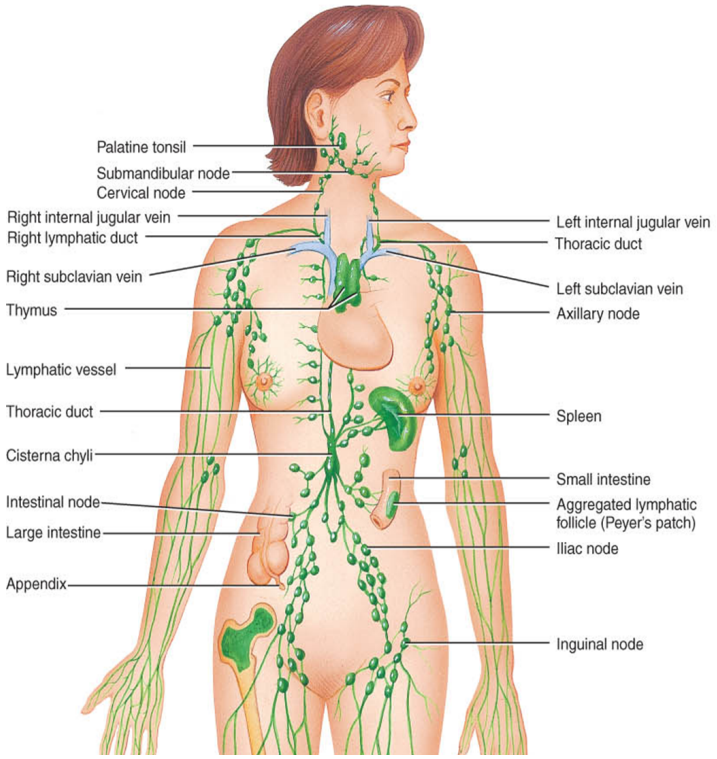

Figure 2.1: The lymphatic system.

lymphoma, depending if it is fast or slow growing [2]. NHL is further divided into at least 61 subtypes, where diffuse large B-cell lymphoma (DLBCL) (B-cell, aggressive lymphoma) include 30% and follicular lymphoma (FL) (B-cell, indolent lymphoma) include 22% of the cases of NHL [42] [20]. NHL may start in lymph nodes, in specialized lymphatic organs like the spleen or in lymphoid tissue, as found in the stomach and intestine [2]. As the lymphocytes can circulate in lymphatic and blood vessels, the disease may spread to any part of the body.

Nodal lymphomas affect lymph nodes or the spleen, while extranodal lymphoma mainly affects any other site, like gastrointestinal tract, lung, brain, skin or kidneys.

In Norway there were 657 cases of HL in the period from 2008 to 2012, and 4593 cases of NHL [37]. Five-year relative survival for the same period was 87.0 and 69.9 for HL and NHL, respectively.

Biopsy is always done to diagnose and determine the subtype of the lymphoma, and an imaging modality is used to examine the extent of metastases, which determines the stage of the lymphoma, and the aggressiveness of the tumors. The use of the different imaging modalities for lymphoma staging will be discussed, but first some theory of PET, MR and CT will be presented.

2.2 PET

PET is a functional imaging modality widely used in oncology which provides metabolic information, but has also applications in neurology and cardiology [5]. A radionuclide is attached to a tracer, a radiopharmaceutical, and injected into the patient a specific time interval before data acquisition [58]. The tracer will guide the radionuclide to the site of interest and the radiation induced by the radionuclide will be detected by the PET detectors surrounding the patient and this data is used to create the PET image.

The radionuclide used in PET is a positron emitter, which has an excess of protons in the nucleus and decay by positron (β^+) decay. A proton in the nucleus is converted to a neutron to make the nucleus more stable, and a positron (a positive electron) and a neutrino are emitted [58]. As the positron leaves the atom it will interact with the surrounding tissue by elastic and inelastic interactions with atomic electrons and nuclei [5]. This cause changes in the direction of the positron and the inelastic interactions cause transfer of the positron's energy to the surrounding tissue. The positron will eventually come to rest and it may combine with an electron, also at rest, and they will annihilate. During annihilation, their masses are converted to electromagnetic energy, in the form of two photons with an energy of 511 keV each, corresponding to the mass of the positron and the electron to conserve the energy [14]. The two photons will travel in opposite direction, 180° apart, to conserve the momentum. If the positron and electron is not completely at rest at the time of annihilation, they will deviate from the 180° (in average by $\pm 0.25°$).

If the annihilation photons manage to escape from the body, they can be detected by the PET detectors, surrounding the patient. The detection of the two photons is used to make a line-of-response (LOR) between the two detector elements involved, which will intersect the annihilation site as the photons (are assumed to) travel in opposite directions. The LOR is counted in a sinogram, which is a matrix where each row correspond to the angle of the LOR, ϕ, and each column corresponds to the radial distance, r, from the LOR to the center of the detector rings, as seen in Figure 2.2. The tracer is assumed to be somewhere along the LOR, but as the positron travels a distance (typically between 10^{-1} and 10^{-2} cm) before the annihilation and the two photons may not be precisely collinear, this is not exactly true, which produce an uncertainty in the spatial position of the tracer.

If the two annihilation photons are detected within a certain time window (e.g. 4.1 ns), have an energy within a selected energy window (e.g. 435-650 keV) and the two detectors are within a valid acceptance angle (e.g. 13.2°), a new count is registered for that LOR in the corresponding matrix element in the sinogram [5]. The sinogram is used to reconstruct the image, by analytic reconstruction, like filtered-backprojection (FBP), or iterative reconstruction, like ordered subset expectation maximization (OSEM). For FBP, each projec-

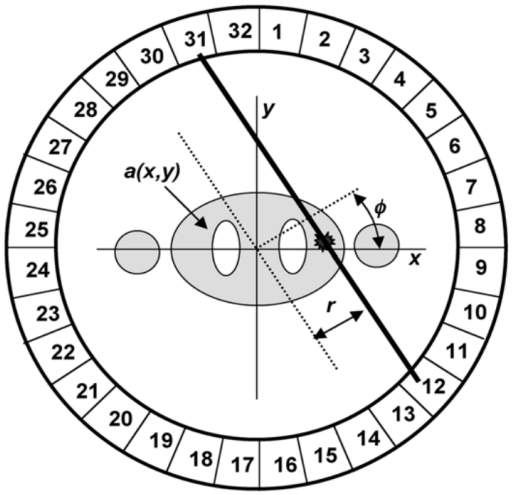

Figure 2.2: A line-of-response (LOR) with its corresponding angle ϕ and distance r from the center of the detector ring [14].

tion (a row in the sinogram) is backprojected into the image, which means that each pixel will get an intensity corresponding to the number of registered LORs intersecting that pixel and the length of the LORs inside that pixel.

In iterative reconstruction, the algorithm first assumes an image, which usually is an uniform image [14]. The assumed image is then forward-projected (the inverse of back-projection) to get the corresponding sinogram. The measured sinogram is then compared to the sinogram of the assumed image by the cost function, which is a measure of the difference or similarity between them. The cost function should be minimized or maximized, respectively, during the reconstruction. The assumed image is updated by an update function, and the process is iterated several times, or until a threshold of the cost function is reached, and the assumed image finally constitute the reconstructed image.

The position of the annihilation can be better estimated by the use of time-of-flight (TOF). The time difference, Δt, between the arrivals of the two annihilation photons at the detector, is then used to better locate the position within a smaller range along the LOR [14]. The position is calculated as the distance d from the midpoint of the LOR,

$$d = \frac{\Delta t \cdot c}{2}, \tag{1}$$

where c is the speed of light (30 cm/ns). A good timing resolution is needed to utilize TOF, and the uncertainty in the position is dependent on the timing resolution of the scintillator. The LSO crystal of the Biograph mCT scanner (Siemens) has a timing resolution of 555 ps, which gives an uncertainty in the position of 8.3 cm along the LOR. TOF is not available at the Biograph mMR scanner (Siemens), as the detector used have a slow response time and the small output signal requires amplification prior to processing [57].

In addition to uncertainties in the emission process (positron range, non-collinearity of the photons), the spatial resolution is also influenced by physical factors in the detection process, e.g. the finite size of the crystals, the depth of the interaction and scatter inside the scintillator [47]. Due to the ring geometry of the detector, the detector blocks are increasingly tilted with increasing distance from the center of the ring [11]. This cause an increased incident area of the detector blocks away from the center and the point response, which is represented by the point spread function (PSF), gets broader. The spatial invariant PSF is usually measured at a great number of points in the tomograph and compensated for in the reconstruction. The contrast of small lesions is then improved [4].

2.2.1 Attenuation correction and scatter correction

Before reconstruction, several corrections of the raw data must be performed in order to obtain quantitatively correct images. The most important corrections are attenuation correction and scatter correction. The two photons created during annihilation inside the patient, will travel through several types of tissue (and possibly obstacles inside the scanner bore) before the detector is reached. There exist a relatively high probability that the annihilation photons with an energy of 511 keV will interact with the tissue, mostly by Compton interactions [14]. Some of the photon's energy is then transferred to a free or loosely bound atomic electron, which is ejected and the photon is scattered, its direction is changed. The reduction in energy may cause the photon to not reach the detector, especially photons originating from deeper tissue. The lack of detections and the scattering of the photons must be compensated for, which is done by attenuation correction and scatter correction, respectively.

An attenuation map (μ-map) is made for attenuation correction, where each pixel represent the probability of interaction per unit distance travelled by the 511 keV photons, called linear attenuation coefficient (LAC) or μ [14]. Also LACs for all fixed objects inside the scanner, like beds and coils (for MR imaging), can be included in this map. For stand-alone PET scanners, the μ-map is made from a transmission scan, where rod sources circulate around the patient, and a blank scan without the patient. In PET/CT and PET/MR scanners the attenuation maps are made from a low-dose CT image and usually from MR images, respectively. These methods will be further described in

following sections. The attenuation map is multiplied with the sinogram before reconstruction, to correct for attenuation.

If none of the two photons from the same annihilation is scattered, and they both reach the detector and are accepted as a LOR according to the criteria, this event will constitute a true coincidence, as seen in Figure 2.3. If one or both of the photons detected as a LOR are scattered, this is called a scattered coincidence which will cause an incorrect LOR that produce noise in the image. If two photons from distinct annihilations reach the detector within the time window and are within the criteria, this will cause a random coincidence, also producing an incorrect LOR. If more than two photons are detected within the same time window, a multiple coincidence, the coincidence will be discarded.

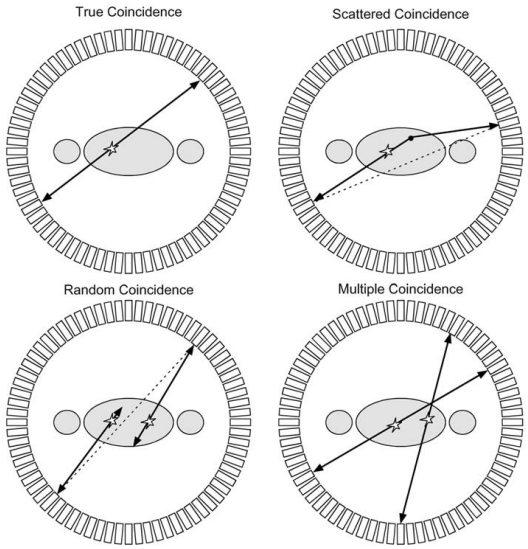

Figure 2.3: True, scattered, random and multiple concidences [13].

The contributions from scattered coincidences are reduced by the use of an energy window (usually 435-650 keV), as scattered photons have lower energy. In addition, scatter correction is performed, by different approaches, for instance by simulations based on the sinogram data and the μ-map. The scatter correction should be done before the attenuation correction [14].

2.2.2 The PET detector

A PET detector is usually made by several detector rings (4 on the Biograph mCT), which consists of detector blocks. These blocks are made of scintillation material, which are cut into smaller elements divided by reflecting material, as seen in Figure 2.4 [14]. When a photon interacts with the scintillation material, the photon will be absorbed by the scintillator, which is excited and isotropically emits light photons, proportional to the energy of the annihilation

photon. Four photomultiplier tubes (PMTs) are usually placed behind one detector block, which convert the incoming light into an electric current. A light photon that enters a PMT will excite a photocathode, and an electron will be emitted with a probability of 15% to 20%. The electron will be accelerated by a potential difference and hit several dynodes on the way, which emits 3-4 electrons per incident electron, inducing a cascade of electrons and produce an easily detectable current at the PMT output. Each incoming annihilation photon produce an electric pulse with an amplitude determined by the number of light photons emitted by the scintillator, hence proportional to the energy of the annihilation photon.

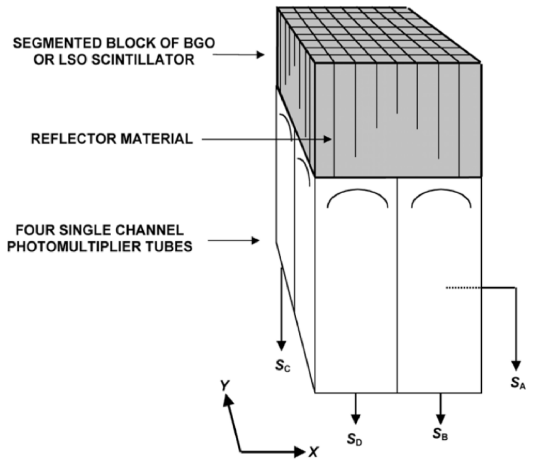

Figure 2.4: A detector block, scintillator material is cut into smaller segments and connected to four PMTs [14].

The distribution of the light photons among the four PMTs is used to determine the position of the incident annihilation photon [14]. The saw cuts in the middle of the block are shallow so that the light photons entering here are more uniformly spread among the four underlying PMTs. The saw cuts are deeper at the edges of the block, to direct the entering light photons mostly to one PMT. The coordinates of the incoming photon are determined by the signal from the four PMTs, S_A, S_B, S_C, S_D, as

$$X = \frac{S_A + S_B - S_C - S_D}{S_A + S_B + S_C + S_D} \qquad Y = \frac{S_A + S_C - S_B - S_D}{S_A + S_B + S_C + S_D} \tag{2}$$

PMTs are usually implemented in stand-alone PET scanner and the earlier generation PET/CT scanners. Digital PET detectors (SiPM, APD) are now replacing PMTs in new PET/CT scanners, and are used in PET/MR scanners as these detectors are not affected by the magnetic field of the MR scanner. These detectors are further explained in *2.6.2 Detectors*.

2.2.3 PET tracers

Many tracers are used in PET imaging, but a fluorinated glucose analog, ^{18}F-FDG, is most used as it is a very effective and powerful radiopharmaceutical. Other tracers are for instance ^{15}O-water, ^{13}N-ammonia and ^{82}Rb, which are widely used for myocardial blood flow imaging [24]. The half-life (the time it takes for half the nuclei in a sample to decay) of ^{18}F is relatively long, 109.8 min, which is convenient as the tracer is often transported a distance from the production cite, the cyclotron, to the hospital.

^{18}F-FDG is widely used for staging, recurrence assessment and follow-up in oncology, as tumors have an increased uptake of glucose compared to normal tissue as the metabolic rate is abnormally high [31]. However, this tracer can also be used to study brain metabolism, cardiac function and sites of infection. ^{18}F-FDG is given to the patient intravenously approximately 60 minutes before the PET acquisition to be distributed in the body and transported into cells by glucose membrane transporters, before imaging. Inside the cell, FDG is phosphorylated to FDG-6-phosphate which will stay in the cell as it is not able to enter the glycolysis or leave the cell. As tumor cells have an increased number of glucose transporter molecules and a low concentration of glucose-6-phosphatase, they will accumulate ^{18}F-FDG.

The uptake of ^{18}F-FDG is also dependent on factors like the blood glucose level, tissue oxygenation, regional blood flow, fat and muscle volume, recent activity and body temperature. It is therefore important that the patients fast for a period (6 h) before the examination, and are relaxed and not freezing after the injection of the tracer. ^{18}F-FDG is not a tumor-specific tracer and is also taken up by glucose consuming organs like the heart, brain and kidneys, and is excreted by the bladder which also shows an increased uptake [31]. Inflammations may also cause an increased uptake of ^{18}F-FDG, which can be present in tumor cells or in the surrounding tissue, as a result of radiation therapy or chemotherapy.

2.2.4 Semi-quantitative measurement in PET: Standardized uptake value

For quantification of the ^{18}F-FDG uptake in PET imaging, standardized uptake value (SUV) is normally used [42], which is a semi-quantitative measure of the FDG uptake [5], and hence an estimate of glucose metabolic activity. In the clinic, PET staging is usually performed only by visual evaluation of the PET images or visually together with SUV measurements. SUV can provide additional information about the aggressiveness of the tumors, which can be taken into account during the visual evaluation [64].

SUV is also used to quantify treatment response [42], especially in early treatment response when anatomical changes may not be visible [4]. Clinical

studies have found a decrease in SUV by 20-40% in most tumors responding to therapy, early in the treatment course [4]. SUV is calculated as

$$\text{SUV} = \frac{\text{c}}{(\text{A/w})} \tag{3}$$

where

$$A = A_0 e^{-\lambda t},\ \lambda = \ln 2/\text{t}_{1/2}, \tag{4}$$

c is the measured activity (e.g. mean, maximum) in a region-of-interest (ROI) in the image [kBq/ml], A is the injected activity of ^{18}F-FDG corrected for decay [MBq] and w is the body weight of the patient [kg] [33]. A_0 is the injected activity at the time of injection, t is the time between injection and imaging (uptake time) and $t_{1/2}$ is the half-life of the radionuclide. If it is assumed that 1 ml of tissue weighs 1 g, SUV is dimensionless. Other measures than weight, lean body mass or body surface area, may also be used as an estimate of the volume distribution of the tracer, w. Weight is mostly used, however, lean body mass or body surface area may be better in some cases, for instance if weight differ a lot from one examination to the next. Weight reduction due to the disease is not that often seen in lymphoma patients as for lung patients, for instance, and it is therefore not a problem to use weight in the SUV calculations in lymphoma patients.

The use of SUV to diagnose tumors is not widely accepted, as there is a large variation in the value due to potential physical and biological errors, and variations in acquisition, corrections and reconstruction [33]. Inflammations and infections may have a high SUV and indolent or slowly developing malignant sites may have a low SUV. For these reasons, SUV must be used with care and biological factors and imaging parameters should be kept as constant as possible.

Reference measurements are usually done in the aorta and the liver of the patient, to check that the FDG uptake in general is not abnormally high or low [40]. The SUV in the liver should be in the interval 2-4, and SUV in the aorta about 1 below the liver value.

SUV is usually calculated from the mean or maximum activity in a ROI, SUVmean or SUVmax, which both have advantages and disadvantages. SUVmean may not be a proper way to measure SUV due to image noise and the limited resolution of PET images which makes the delineation of the tumor challenging and physician-dependent [33]. However, as the measurement is obtained from several voxels, it is less sensitive to noise [4]. Partial volume effects can cause errors in the measure of SUVmean if the region is less than approximately 3 cm, hence the ROI should be placed in the central part of a relatively large lesion, and the distribution in the lesion should be uniform.

In a small lesion, SUVmax is a more precise estimate of the true SUV, and is found to be more reproducible than SUVmean [33]. However, SUVmax is

highly dependent on statistical noise in the image and the size of the image pixel [61]. SUVmax is more used than SUVmean, since it is less dependent on the physician and more reproducible [4], and it is shown in several studies that SUVmax is a good measure for treatment response [33]. SUVmax represent the site of strongest glucose metabolism within the tumor and is correlated with tumor aggressiveness and prognosis [55].

Another measure, SUVpeak, was introduced to maintain the advantages of SUVmean and SUVmax, the noise reduction and the reproducibility, and is recommended by some groups [4]. SUVpeak is the mean SUV in a ROI of fixed volume (for instance 3x3 pixels or 1 cm^3), centered at the maximum pixel in a lesion.

To summarize, the SUV measurements are:

- SUVmax: maximum SUV in a ROI representing the lesion
- SUVmean: mean SUV in a ROI representing the lesion
- SUVpeak: mean SUV in a small ROI of fixed volume (3x3 pixels or 1 cm^3) centered at the maximum pixel in the lesion

2.2.5 COV

COV is a measure of image quality, obtained from the reconstructed PET image. COV is measured in a ROI in an area assumed to have an uniform uptake of ^{18}F-FDG, usually in the liver, to evaluate the image quality by the variance in the image. COV is calculated from the mean counts and the standard deviation (std) of the counts in the ROI [36], as

$$\text{COV}(\%) = \frac{\text{std}}{\text{mean counts}} \cdot 100 \tag{5}$$

2.3 MR

MR imaging is an anatomical imaging modality with excellent soft tissue contrast. The patient lays inside the bore of the scanner where a static magnetic field (usually 1.5 T or 3 T), B_0, cause the magnetic moments of the atomic nuclei in the body to be aligned, either along or against the magnetic field [10]. The nuclear spins precess around the B_0 field with a frequency, called the Larmor frequency, found by

$$\omega = \gamma B_0, \tag{6}$$

where $\gamma \approx 42.58$ MHz/T for protons [52]. The proton in hydrogen is the dominant nucleus in MR imaging [23]. The sum of all the magnetic moments cause a net magnetization in the direction of the B_0 field, z-direction, as there is a small excess of nuclei in the parallel state (lower energy level) than in

the antiparallel state (higher energy level). A radio frequency (RF) pulse, B_1, with the same frequency ω as the nuclei, is transmitted orthogonal to the B_0 field to apply a torque on the precessing nuclei. This field force the net magnetization towards the transverse plane, orthogonal to the z-direction. If the magnetization is flipped all the way to the x-y plane, the RF pulse is called a 90°-pulse, as the flip angle is 90°. The net magnetization then precesses in the x-y plane and induces a current in a receive coil which constitute the MR signal, called free induction decay (FID). The flip angle, $\Delta\Theta$, of the magnetization with respect to the z-direction, is determined by the B_1 field and the duration of the RF pulse, τ, as

$$\Delta\Theta = \gamma B_1 \tau. \tag{7}$$

The spins will interact with the surroundings, which will cause energy transfer and decay of the signal as the net magnetization will go back to the z-direction. The time it takes to regrow the magnetization in the z-direction is dependent on the tissue and is represented by the longitudinal relaxation time or spin-lattice relaxation time, T_1 [8]. T_1 is the time it takes before 63% of the net magnetization is regrown in the z-direction.

Due to differences in the local fields for the spins, which is a combination of the external fields and the field produced by the neighbouring spins, they will have slightly different Larmor frequency [23]. Immediately after the RF pulse is transmitted, the spins will be coherent, but as the time pass, they will dephase and the signal will decay, without any energy loss. The time it takes for 63% of the signal to be lost, is the spin-spin relaxation time or the transverse relaxation time, T_2, which is shorter than T_1. T_2 is dependent on local, random and time-dependent field variations.

In practice, inhomogeneities in the external field also cause dephasing and decay of the signal, and this is represented by the relaxation time T_2' [23]. The overall transverse relaxation time, T_2^*, is defined as

$$\frac{1}{T_2^*} = \frac{1}{T_2'} + \frac{1}{T_2} \tag{8}$$

The differences in T_1 and T_2 can be utilized to distinguish different tissue types and make different contrasts in the image by adjusting the different parameters in the various MR-sequences.

2.3.1 Gradients

In order to obtain spatial information, gradient magnetic fields are applied in addition to the static B_0 field, and cause spatial variations in the precession frequency [23]. If a linear gradient, with strength G, is applied in the z-direction, the spins will have a Larmor frequency increasing with the position z, as the magnetic field is linear proportional to z,

$$\omega(z) = \gamma\left(B_0 + zG\right). \tag{9}$$

One gradient is applied during the transmit of the RF pulse, and is called the slice selection gradient ($G_{z,SS}$ in Figure 2.7). The RF pulse has a limited bandwidth and will only excite nuclei with frequencies within that bandwidth, which cause the selection of a slice perpendicular to the direction of the gradient with a certain thickness. The central frequency of the pulse determines the position of the slice, and the thickness of the slice, TH, depends on the bandwidth of the pulse ($\Delta\omega = \Delta f$) and the gradient strength, G, as seen in Figure 2.5.

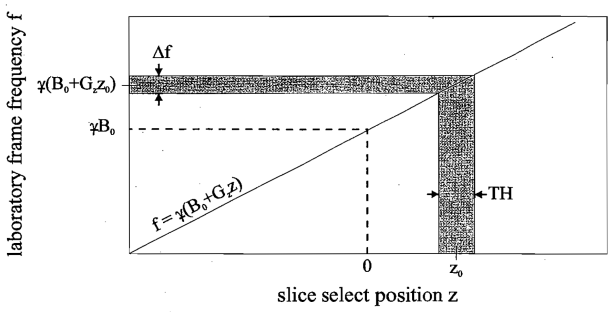

Figure 2.5: The slice thickness, TH, is determined by the bandwidth, Δf, and the strength of the gradient, G [23].

The measured signal, $s(k)$, and the image, $\rho(z)$, are a Fourier transform pair, which means that the Fourier transform, a mathematical tool, can be used to calculate the other when one of them is known [23]. The image can be found by the inverse Fourier transform of the signal by

$$\rho(z) = \int dk\ s(k)e^{i2\pi kz} \tag{10}$$

for a one-dimensional (1D) case.

The measured data are collected in k-space (Figure 2.6), which is in the spatial frequency domain, and the coverage of k-space must be sufficient to do the inverse Fourier transform, to obtain the image [23]. If a constant gradient, G, and a constant time interval, Δt, is used during sampling of the signal, the sample points in k-space will be uniformly distributed with an interval of

$$\Delta k = \underline{\gamma} G \Delta t. \tag{11}$$

Another gradient, called frequency encoding gradient or readout gradient ($G_{x,R}$ in Figure 2.7), is applied during the readout of the signal, perpendicular to the slice selection gradient, to move in the readout direction (k_x) in k-space, as seen in Figure 2.6 [23]. An additional gradient, the phase encoding gradient ($G_{y,PE}$ in Figure 2.7), is applied perpendicular to the other two, before the readout, to move in the phase direction (k_y) in k-space. In order to move

several steps in the phase direction, several RF pulses are transmitted with a time interval called the repetition time, TR, as seen in Figure 2.6, while the strength of the phase encoding gradient is increased for each RF pulse. Movement in the negative direction in k-space can be done by changing the polarity of the gradient.

In this way, k-space is discretely sampled in two dimensions by the readout gradient and the phase encoding gradient, and in three dimensions if this is repeated with increasing/decreasing slice selection gradient. A discrete inverse Fourier transform can be used if the sample points in k-space are on a rectangular grid, symmetrically distributed around the origin. If the sample points are not sampled on a rectangular grid, they can be interpolated to such a grid afterwards. Different sampling approaches are used, and modifications can be done after sampling to obtain a symmetric distribution in k-space. As

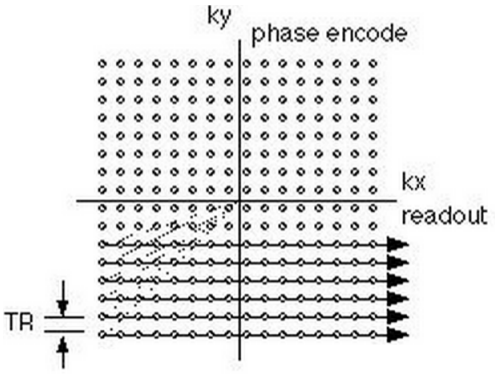

Figure 2.6: K-space. The readout gradient cause movement in the readout direction (k_x), and repeated RF pulses with increasing strength of the phase encoding gradient cause movement in the phase direction (k_y) [15].

the signal will be sampled discretely and during a finite amount of time, a discrete Fourier transform will be used, instead of the continuous transform in equation 10. The discrete sampling cause a limited field of view (FOV) and the truncated data cause a limited spatial resolution of the image and potentially artifacts in the image [23].

2.3.2 MR sequences

The two most basic sequences used in MR imaging are the spin echo and the gradient echo sequence [23]. The FID signal following a 90°-pulse is dephased relatively fast, and a 180°-pulse or a gradient can be used to rephase the spins to get an echo and easier measure the signal.

In the spin echo sequence a 90°-pulse is followed by a 180°-pulse, as shown in Figure 2.7. The 180°-pulse flips the spins 180°, and the spins with highest frequency will catch up with the spins with slower frequencies and create an

echo. The echo will occur at the time TE (the echo time), when the time interval between the two pulses is $TE/2$. Magnetic field inhomogeneities are eliminated by the 180°-pulse and the echo decays by T_2 effects.

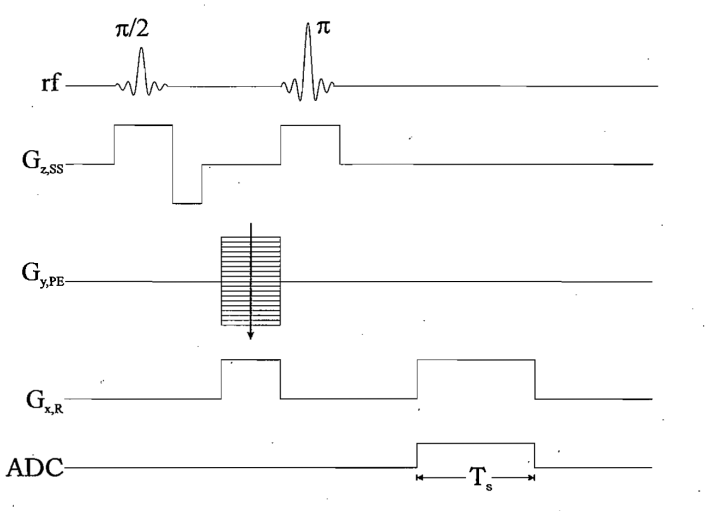

Figure 2.7: Sequence diagram for a two-dimensional (2D) spin echo imaging sequence [23]. A 90° ($\pi/2$) and a 180° (π) RF pulse is transmitted, which are sinc pulses in the time domain. The slice selection gradient ($G_{z,SS}$) is applied during the RF pulses. The phase encoding gradient ($G_{y,PE}$) is applied before readout, with decreasing strength for each repetition (causing movement in the positive phase direction, due to the 180°-pulse), and the readout gradient ($G_{x,R}$) is applied during readout. The readout is represented by the analog-to-digital converter (ADC), and have a duration of T_S. The negative lobe at the slice selection gradient is applied to rephase the dephasing that occurs during the RF pulse. The first lobe at the readout gradient is applied to move in the negative direction in the readout direction (inversed by the 180°-pulse), so that the readout is symmetric about the k_y-axis.

In the gradient echo sequence, a flip angle usually below 90° RF pulse is applied. The readout gradient is used to increase the frequency differences of the spins to dephase the signal, and then changing the polarity of the gradient to rephase the spins and construct an echo (Figure 2.8). The gradient echo do not rephase static magnetic inhomogeneities, and hence decays by T_2^* effects.

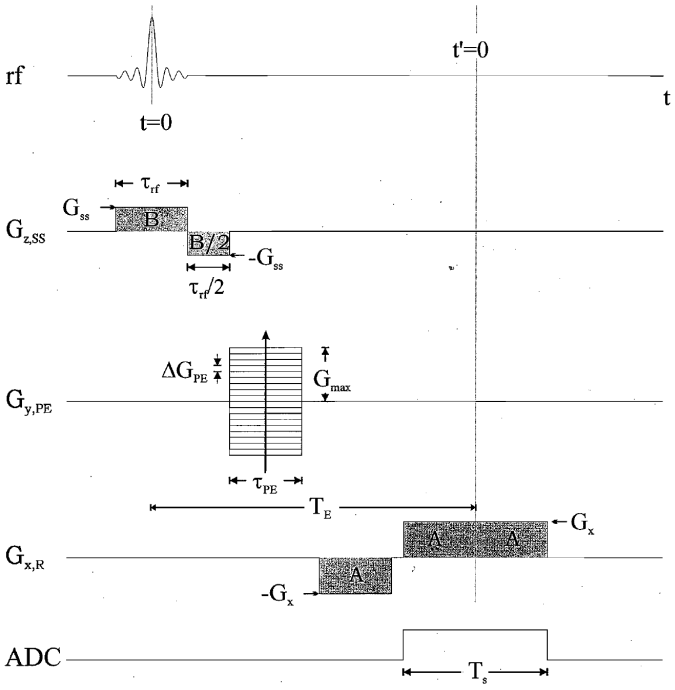

Figure 2.8: Sequence diagram for a 2D gradient echo imaging sequence [23]. A 90° ($\pi/2$) RF pulse is transmitted, which is a sinc pulse in the time domain. The slice selection gradient ($G_{z,SS}$) is applied during the RF pulse. The phase encoding gradient ($G_{y,PE}$) is applied before readout, with increasing strength for each repetition (causing movement in the positive phase direction). The signal is dephased by the negative readout gradient ($G_{x,R}$) lobe and rephased by half the positive lobe and an echo is formed at time t'=0. The readout is represented by the ADC, and have a duration of T_S. The negative lobe at the slice selection gradient is applied to rephase the dephasing that occurs during the RF pulse.

2.3.3 Diffusion weighted imaging and apparent diffusion coefficient - a MR quantitative measurement

Random thermal motion (Brownian motion) cause the molecules in a fluid or gas to move, a motion called diffusion, which is characterized by the diffusion coefficient, D, given in mm^2s^{-1} [8]. In diffusion weighted imaging (DWI), the diffusion of hydrogen nuclei in the body (in different types of tissue) is used to make the contrast in the MR images, and we can use the images to calculate the diffusion coefficient in the body.

In a DWI sequence, two symmetric gradient pulses are applied before and after the 180°-pulse in a spin echo sequence [32]. Stationary spins will then be dephased and fully rephased by the two gradient pulses and produce a high signal. Spins that are moving in the same direction as the gradient, will not be fully rephased at the echo time, which reduce the signal and produce a lower intensity in the image. If $S(0)$ is the original signal amplitude, the DWI sequence will produce a signal amplitude equal

$$S(b) = S(0)e^{-bD} \tag{12}$$

where

$$b = \gamma^2\delta^2G^2(\Delta - \delta/3), \tag{13}$$

δ is the duration and G is the amplitude of the gradient pulse, and Δ is the time between the two gradient pulses as seen in the sequence diagram in Figure 2.9. b represent the signal sensitivity to motion, as the signal loss due to diffusion will increase as b increase.

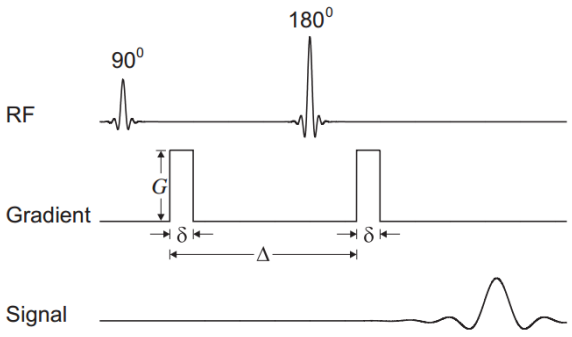

Figure 2.9: A DWI sequence, consisting of a spin echo sequence with diffusion sensitive gradients applied before and after the 180°-pulse. G is the amplitude and δ is the duration of the gradient pulses, and Δ is the time interval between the two pulses.

From two or more diffusion-weighted images with different b-values (for instance $b_1 = 50$ mm^2s^{-1} and $b_2 = 800$ mm^2s^{-1}), an image called an ADC map

can be calculated as

$$\mathrm{ADC} = -\frac{\ln(\mathrm{S}_1/\mathrm{S}_2)}{\mathrm{b}_2 - \mathrm{b}_1} \tag{14}$$

where

$$S_1 = S(0)e^{-b_1 D} \tag{15}$$

$$S_2 = S(0)e^{-b_2 D}. \tag{16}$$

Regions with a low ADC value will have a restricted diffusion, while freely moving spins have a high ADC value.

For lymphoma patients ADC values can be used to study if the diffusion in the lymph nodes is restricted due to high density of cancer cells. ADC is a marker for tumor microstructure [17] and detects microscopic changes in mobility of water [16]. The minimum ADC value in a tumor, ADCmin, represents the most malignant site within the tumor [64]. ADC can reflect the effect of anti-cancer treatment, which may cause the cell membrane to rupture and cell necrosis which increase the water mobility and hence increasing ADC values.

2.4 CT

CT is an anatomical imaging modality, where x-rays are emitted from a source and pass through the patient. The photons are attenuated by the tissue and detected by detectors on the opposite side, if their energy is sufficient [54]. The transmission of the x-rays or the attenuation coefficients are calculated from electrical signals from the detectors. In todays CT scanners the source and the detector is usually rotated continuously while the patient is moved through the scanner, which is called spiral CT (Figure 2.10). The x-ray beam is usually fan shaped (or may be cone shaped), and one rotation takes about a second or less.

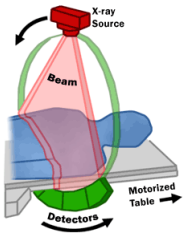

Figure 2.10: Principle of CT. A fan beam of x-rays are rotated around the patient while the table is moving.

Scintillator detectors, coupled to PMTs or photo-diodes, are used in almost all CT scanners today [9].

CT is used for diagnosis of diseases, for imaging of traumas and other abnormalities. It is also used in planning of interventions and radiation therapy, and for monitoring therapy response. CT has many advantages, the examination is fast and standardized, and it is excellent for bone imaging. Still, the soft tissue contrast is limited and the radiation doses for diagnostic whole-body imaging is high (over 10 mSv) [10].

2.5 PET/CT

The first integrated PET/CT system was introduced in 1998 and was used in the clinic from early 2001 [59]. Today, PET/CT scanners have replaced the standalone PET scanners [18], as the CT scan provides a faster attenuation correction and anatomical information. During a PET/CT examination, a fast, low-dose CT scan is followed by the PET scan (in addition to diagnostic CT when acquired) [59]. The functional PET image can be fused with the anatomical CT image to better locate lesions found in the PET image. As mentioned, PET/CT is an important tool for diagnosis, staging and therapy monitoring in oncology.

2.5.1 Attenuation correction

In PET/CT scanners, an attenuation map (μ-map) is made from the low-dose CT image by transformation of the Hounsfield units (HU) in the CT image (which is usually for energy around 70 keV) to attenuation coefficients for 511 keV photons by a bilinear curve, shown in Figure 2.11.

CT-based attenuation correction is considered as the gold standard in attenuation correction [10], as transmission scans are noisier and more time consuming than low-dose CT images [5]. A PET/CT examination is performed about 25-30% faster than an examination at a stand-alone PET scanner.

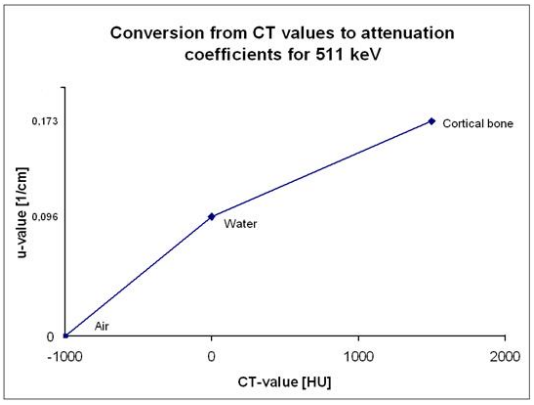

Figure 2.11: Bilinear curve for transformation from CT Hounsfield units to attenuation coefficient for annihilation photons of 511 keV.

2.6 PET/MR

The combination of PET and MR has been challenging, as the two modalities have detrimental effect on each other's performance [10]. Especially the development of PET detectors capable to operate in a magnetic field, has been time consuming process.

The first simultaneous PET/MR examination of a patient (human brain) was performed in 2006, where a MR compatible PET detector ring was placed inside a MR scanner [51], and the first clinical simultaneous whole-body scanner was introduced in 2010 [19]. In Norway, there is one PET/MR scanner, installed autumn 2013, which is still only used for research.

2.6.1 Attenuation correction

The attenuation correction in PET/MR is quite challenging, as the MR image represent the proton density and tissue relaxation properties rather than electron density, which the attenuation is proportional to [42]. Both air and cortical bone give no signal in a conventional MR image, however, air does not attenuate the annihilation photons whereas bone have the highest attenuation coefficient in the body [6]. Incorporation of CT-based attenuation correction in the PET/MR scanner is not an option as the space is limited and due to crosstalk between CT and the magnetic field.

Different approaches are used to perform attenuation correction based on MR images; template-based, atlas-based, and segmentation-based approaches based on special MR sequences [60].

For the template-based approach, an attenuation map template is made based on several PET transmission scans and a co-registered MR template [60]. The MR template is registered to the patient MR image and the same nonlinear transformation is done for the attenuation map template, which can then be used for the attenuation correction for that patient.

The atlas-based approaches use an atlas that usually consists of a set of MR images with matched CT images. The MR atlas data sets are nonlinearly adapted to the MR image of the patient, and this spatial transformation is also done to the CT atlas data sets. From this, an average CT image is generated for attenuation correction. These two methods are best suited for regions with low anatomical variability, like the brain [18].

Segmentation-based approaches segment an MR image into different tissue classes and assign them with a predetermined attenuation coefficient value. The most used method generate separate images of water and fat by a two-point Dixon-sequence and segment whole-body MR images into lungs, fat, soft tissue and air/background. For this sequence, no signal is obtained from bone, which may cause underestimation of the PET signal in areas with a lot of bone.

However, ultrashort echo time (UTE) sequences can be used to visualize

and include bone in the attenuation correction, which has a very short spin-spin relaxation time, T_2. An image with a longer TE is compared to an image with ultrashort TE, and bone is detected as areas that produce signal in the image with ultrashort TE, but not in the image with longer TE[29]. This method seems promising for the brain [3], but is too time consuming for whole-body imaging as the acquisition time is around 2 minutes per bed position.

The segmentation-based methods are robust and fast, but atlas methods may be more accurate for quantitative PET measurements [6].

The FOV is limited in MR, mainly due to the homogeneity of the static magnetic field and the linearity of the gradient fields [45]. Therefore, the patient is usually not fully covered in the transaxial direction in MR scanners, and the arms are not included in the image (can also be the case for hips and breasts). This may cause truncation artefacts, which will affect MR-based attenuation maps, if it is not corrected for [18]. The missing body parts can for instance be outlined by the uncorrected PET data and added to the attenuation map, which are methods that are available at clinical scanners.

As mentioned, fixed objects in the scanner, like the bed and head coils, are included in the attenuation correction by including μ-maps, created by CT images, which are stored at the scanner. Other objects, like surface coils and headphones, can still not be included in the attenuation correction, even though it has been attempted.

2.6.2 Detectors

The combination of PET and MR in one scanner induced several problems. The light yield of the scintillator material, the electrons in the PMTs and the front-end electronics of PET are all affected by the static magnetic field, the gradient fields and the RF pulses of MR [10]. Furthermore, the PET detectors can cause inhomogeneities in the magnetic field and degrade the image performance of the MR system. To solve some of these issues, scintillators suited for magnetic fields have been developed, and the PET electronics are shielded to avoid electromagnetic interference. In early designs, the PMTs were placed outside the magnetic field connected by optical fibers [42]. This caused loss of the signal in the fibers, a deteriorated timing resolution and degradation of the energy. Therefore, solid state photodetectors, avalanche photodiodes (APD) or silicon photomultipliers (SiPM), now replace PMTs, as they are not affected by the magnetic field [10]. A block detector with APDs, as used in the Biograph mMR scanner (Siemens), is seen in Figure 2.12.

A voltage is applied across the APD, and a incident light photon from the scintillator may have sufficient energy to release an electron from the silicon of the APD [14]. Due to the high voltage applied, the electron will gain enough energy between the collisions in the silicon to release more electrons, called an avalanche. The electrons will drift towards the anode and the vacancies, called

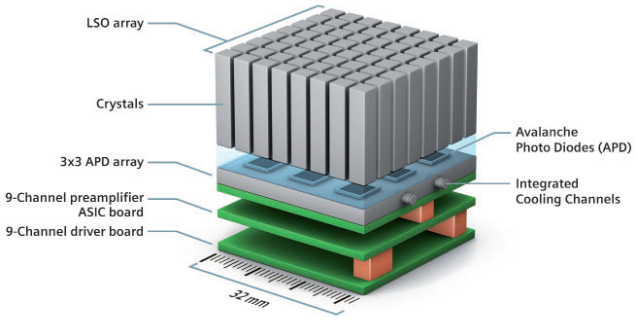

Figure 2.12: A block of the PET detector with scintillator material (LSO) connected to an APD array in the Biograph mMR scanner (Siemens).

holes, will drift towards the cathode. The electric current that is created can be measured, and is proportional to the energy deposited in the scintillator by the incident annihilation photon.

APDs have a higher quantum efficiency (the probability of a light photon to liberate an electron [14]) (up to 80% against 25%, respectively [50]), are more compact and require a lower supply voltage than PMTs. The APDs have a lower signal-to-noise ratio (SNR) than PMTs as the gain is lower ($\sim 10^2$ to 10^3 against 10^6 to 10^7 for PMT), requiring more powerful preamplifiers and hence more cooling, and they have a poorer timing resolution [50].

The SiPM consists of APDs tightly packed on a common silicon substrate, which operate in Geiger mode (their response to excitation is binary) [10]. SiPMs have many of the advantages from both PMTs and APDs as they have a gain that is higher or equal to PMTs, high quantum efficiency, are compact and have a very good timing resolution (less than a nanosecond), which makes them suitable for TOF PET [42].

In the Biograph mMR scanner (Siemens), the PET detector is placed in between the gradient coil and the RF body coil of the MR scanner, as seen in Figure 2.13.

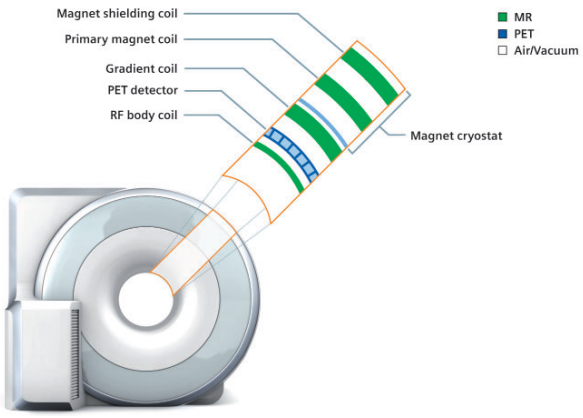

Figure 2.13: The PET detector is placed between the gradient coil and the RF body coil in the Biograph mMR scanner.

2.7 Lymphoma staging

As mentioned, biopsy is performed to diagnose lymphoma and to determine the subtype, while imaging is performed to evaluate the extent of metastases and the aggressiveness of the tumors.

Early and precise staging is important to have a suited therapy for the specific type of lymphoma. CT has been widely used for staging of lymphoma, in addition to bone marrow biopsy [31]. PET was first used for lymphoma staging for more than 20 years ago and ^{18}F-FDG PET is today the standard for staging in state-of-the-art management of HL and high grade NHL, and PET/CT is the most efficient diagnostic tool for initial staging and therapy response [42]. The use of PET/CT for diagnosis and staging of lymphomas has demonstrated a very high sensitivity and specificity in patients with HL and aggresive NHL in most studies, but varying results for indolent lymphomas which may be non FDG avid.

For HL patients, it is shown that PET have a very high sensitivity for nodal staging, and also detects extranodal disease more sensitively than conventional imaging [31]. For approximately 15-25% of the HL patients, more disease sites are detected by PET than conventional imaging, which may lead to a different treatment strategy.

Few similar studies are done for aggressive NHL patients alone, but a study on DLBCL patients showed that PET/CT had a higher sensitivity than CT alone and caused an upstaging of 15% of the patients [31].

^{18}F-FDG PET is not used as much for indolent NHL as sensitivity and specificity seem to vary a lot among studies, still it seems to be useful in addition to other staging tools [31]. Studies also report that ^{18}F-FDG PET can be used for staging of various extranodal lymphoma subtypes, like primary gastrointestinal lymphoma.

Some studies have compared staging of lymphoma based on CT and/or PET with PET/CT and found that the sensitivity is equal for PET/CT compared to CT and PET alone, and that the specificity is better for PET/CT [31].

PET/MR is also showing promising results in lymphoma staging. In a study where PET/MR was used to assess disease burden in lymphoma patients with PET/CT as a reference standard, the sensitivity was found to be similar to PET/CT for identifying FDG-avid nodal groups [26]. PET/MR staging was concordant with PET/CT in 96.4% of the patients, as one patient was correctly upstaged by PET/MR staging due to finding of bone marrow involvement, which was missed with PET/CT staging. DWI staging was also evaluated, and was equivalent with PET/CT staging in 64.3% of the patients, while another study in only DLBCL patients found that DWI staging provided similar results as PET/CT staging [56]. In a study of bone lesions it was found that PET/MR was clinically and technically robust, and that PET/MR was superior to PET/CT for anatomic delineation and allocation of bone lesions [21].

Response to chemotherapy or radiotherapy can be seen in an anatomical image by shrinkage of the tumor, but as morphological changes take time [31], or may not occur, this is no efficient early marker of therapy response [17]. In contrast, metabolic changes (cellular and vascular changes) after therapy are faster and ^{18}F-FDG PET can be used to study these changes which have been found to be highly predictive to the final outcome of the treatment and progression-free survival (PFS) in several studies. SUV can be used to quantify the changes in metabolism, and hence to evaluate therapy response. Clinical studies have shown that most tumors responding to therapy have a decrease in SUV of 20-40% early in the treatment [4]. SUV is also used to assess tumor aggressiveness.

ADC obtained from DWI has also been used clinically to assess tumor aggressiveness, to distinguish benign from malignant tumors, to evaluate tumor extent and to monitor therapy response in various malignancies [46]. Changes in ADC values as a result of therapy are also significantly earlier than morphological changes [12], and ADC may also predict therapy response. A study in HL patients showed that pretreatment ADC was significantly lower in tumor sites with adequate response to chemotherapy, than in sites with inadequate response, while pretreatment SUVmax and nodal volume were not significant different in sites with adequate and inadequate response [44]. Another study in non-small cell lung cancer (NSCLC) patients also found that ADC was better suited for predicting therapy response than SUV [38]. Hence, the combination of PET and MR, providing both SUV and ADC, may be preferred for staging and for predicting and evaluation of therapy response.

Chapter II

Materials and methods

1 Subjects

15 patients with histologically proven lymphoma were included in the current study. The patients were referred to PET/CT at St. Olavs Hospital (Trondheim, Norway) as part of their normal diagnostic routine, and were asked to participate in the study to perform an additional PET/MR examination directly after the PET/CT. No additional dose of ^{18}F-FDG was injected before the PET/MR examination. The study has been approved by the local ethics comittee, REK (Regionale komiteer for medisinsk og helsefaglig forskningsetikk). All included patients gave written informed consent before the PET/CT examination.

One patient was excluded because no lesions with SUVmax above 7 were found in the PET image of PET/MR.

The average weight of the patients was 75±12 kg (range 55-87 kg), the BMI was in average 23.3±2.9 kg/m^2 (range 18.2-26.9 kg/m^2), and the mean age was 55±17 years (range 25-77 years). The injected dose of ^{18}F-FDG was in average 4.00±0.02 MBq/kg (range 3.97-4.03 MBq/kg, average total dose 299±47 MBq, range total dose 220-350 MBq), and the injection was performed 60.3±0.6 min (range 59.5-61.7 min) and 107±13 min (range 90-132 min) before the PET/CT and the PET/MR examination, respectively. The patients were instructed to fast for 6 hours before the examination, and the blood glucose level should preferably not exceed 8-10 mmol/l, and absolutely not exceed 11 mmol/l.

All patients were laid supine and had normal respiration, both for PET/CT and PET/MR. The patients had their arms up for PET/CT scanning and their arms down for PET/MR scanning.

An overview of the lymphoma type, the time of examination (primary/interim) and the number of ROIs made for SUV and ADC analysis for each patient is presented in Table 1.1.

Table 1.1: Overview of the 14 included patients.

Patient number	Nb. of ROIs, PET	Nb. of ROIs, ADC	Primary staging/ Interim	Lymphoma
59	1	-	primary	ALK(anaplastic lymphoma kinase)-negative Anaplastic Large Cell Lymphoma (aggresive NHL)
61	6	-	primary	FL (indolent NHL)
62	1	1	primary	Splenic marginal zone lymhoma (indolent NHL) transformed to DLBCL (aggresive NHL)
65	1	-	primary	FL (indolent NHL)
66	3	-	primary	Mantle cell lymphoma (indolent/aggresive NHL)
67	3	-	primary	FL (indolent NHL) transformed to DLBCL (aggresive NHL)
68	7	1	primary	Angioimmunoblastic T-cell Lymphoma (aggresive NHL)
69	2	1	primary	DLBCL (aggresive NHL)
71	1	-	interrim	HL
72	4	2	primary	HL
73	1	-	interrim	HL
74	3	-	interrim	FL (indolent NHL) transformed to DLBCL (aggresive NHL)
75	8	1	primary	HL
76	1	1	primary	Mantle cell lymphoma (indolent/aggresive NHL)

2 Image acquisition

2.1 PET/CT

PET/CT examinations were performed on a whole-body Siemens Biograph mCT scanner (Figure 2.1 a) (Siemens Healthcare Erlangen, Germany). The protocol consisted of a low-dose CT scan and a multi bed position (7-14) PET scan.

Figure 2.1: **a)** The Biograph mCT scanner. **b)** The Biograph mMR scanner.

The CT images covered head to thigh, except for one patient where head to

toe was covered. The CT scan was done in caudocranial direction and the slice width was 3.0 mm. All patients were scanned with a peak tube voltage of 120 kV, a rotation speed of 0.5 s and a pitch of 0.95. The collimation was 64x0.6 mm and the reference tube current-exposure time product was 40 mAs. The CT image was used for attenuation correction of the PET image.

The PET acquisitions consisted of 7 or 8 bed positions, covering the head to thigh, except for one patient with 14 bed positions covering head to toe. The overlap between the bed positions were 41 %, and the acquisition time was 150 s per bed position. The acquisition was done in 3D mode, and an OSEM algorithm was used for reconstruction, with 2 iterations and 21 subsets. TOF and PSF was used, the image matrix consisted of 256x256 elements and the image was filtered with a Gaussian filter with Full-Width Half-Maximum (FWHM) of 4 mm. The typical sensitivity of the system is 10.2 kcps/MBq.

The PET detector is made up of 4 detector rings, where each ring consists of 48 block detectors. Each block contains scintillator material, which is a lutetium oxyorthosilicate (LSO) crystal with a size of 4x4x20 mm, in a 13x13 array connected to a 2x2 PMT array. The FOV is 22.1 cm in the axial direction and 70 cm in the transaxial direction. The energy window was set to 435-650 keV, and the coincidence window was 4.1 ns.

2.2 PET/MR

PET/MR examinations were performed at a whole-body Siemens Biograph mMR scanner (Figure 2.1 b) (Siemens Healthcare, Erlangen, Germany).
The protocol consisted of a MR localizer, followed by simultaneous PET and MR acquisition, as shown in Figure 2.2. Five bed positions were acquired for both the PET and MR acquisition, from head to thigh, except for two patients with only one (pelvis) and four (neck to thigh) bed positions, respectively.

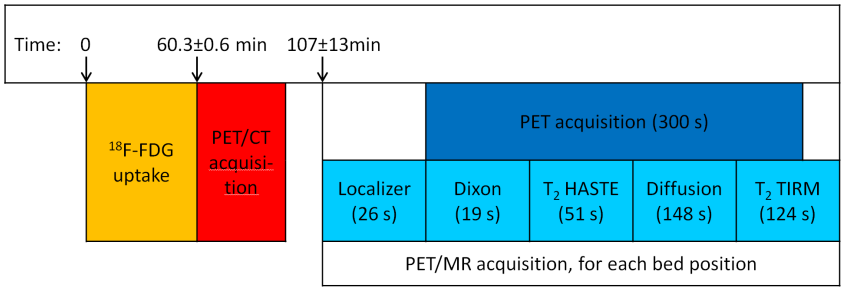

Figure 2.2: Time line of the examinations.

The MR acquisition included a Dixon sequence, a T_2-weighted HASTE sequence, a diffusion-weighted sequence and a T_2-weighted TIRM sequence. The parameters of the MR sequences are presented in Table 2.1.

Table 2.1: Parameters of the MR sequences.

Sequence	TR (ms)	TE (ms)	Flip angle (deg)	Acq. time (s)	Image matrix	FOV read (cm)	FOV phase (cm)	b-values (s/mm^2)
Dixon	3.6	1.23, 2.46	10	19	192x126	50	32.9	
T2 HASTE	1600	95	120	51	320x320	35	35	
Diffusion	5100	59		148	129x112	40	35	50, 800
T2 TIRM	2780	82	120	124	384x348	45	40.8	

The two-point Dixon sequence was used to separate water, fat, in-phase and out-of-phase images, and was used to create the μ-map with four tissue classes (lung, fat, soft tissue, air/background) for attenuation correction. The T_2-weighted HASTE sequence and the T_2-weighted TIRM sequence were used for anatomical imaging, and ADC maps were calculated from the diffusion-weighted images (with b-values of 50 s/mm^2 and 800 s/mm^2).

The PET acquisition time was 300 s per bed position and the overlap of the bed positions was 23 %. The acquisition was done in 3D mode and the OSEM algorithm was used for reconstruction, with 3 iterations and 21 subsets, and with PSF. An image matrix of 344x344 was used and a Gaussian filter with FWHM of 4 mm. The typical sensitivity for this system is 13.2 kcps/MBq.
The scanner has a magnetic field strength of 3 T, with a maximum gradient amplitude of 45 T/m and a maximum slew rate of 200 T/m/s. The maximum applied RF field strength is 23.5 µT and the transmit amplifier bandwidth is 800 kHz.

The PET detector consists of 8 detector rings, which contains 56 detector blocks each. Each block is made up of 8x8 LSO crystal elements with a size of 4x4x20 mm, which is connected to a 3x3 APD array. The transaxial FOV was 58.8 cm and the axial FOV was 25.8 cm. The energy window was set to 430-610 keV and the coincidence window of the scanner is 5.86 ns.

3 Image analysis

The software Vinci (version 4.41.0.15274) was used to define/draw ROIs in the lesions. After making the ROIs, both ROIs and images were transferred to MATLAB R2014b (8.4.0.150421) 64-bit (win64), which was used to perform quantitative calculations of SUV and ADC values.

3.1 SUV

Potential lesions for SUV analysis were found by using a threshold tool to show areas with a SUV above 7, which was used as a guideline to avoid inflammations and infections, as recommended by a nuclear medicine physician. SUV values

in lymphoma lesions usually are much higher than the SUV in the liver (2-4). The lesions that were easily recognized as the same lesions on both PET images, from PET/MR and PET/CT, were included in the analysis. Hence, the same lesions were included from PET/MR and PET/CT. A threshold of 42% of the maximum value in the lesion was used to delineate the lesions in both PET images by the threshold tool, which made up a ROI for the lesion for the SUV analysis. Some small adjustments were done to include approximately the same areas of the tumor on both PET images.

To check for abnormal FDG uptake, reference SUV measurements in the aorta and the liver were performed. An approximately spherical ROI was placed in the aorta and in the liver of the PET images of each patient (except for one patient with only one bed position over the pelvis), with a radius of 3.5 mm and 15 mm, respectively. For PET/MR, the water image from the Dixon sequence was linked to the PET image and used to place the ROI in the middle of the aorta. For PET/CT the same was done by linking the PET image to the CT image.

SUVmax, SUVmean and SUVpeak were measured in all ROIs in the PET images of PET/CT and PET/MR, called $\text{SUVmax}_{\text{CT}}$, $\text{SUVmean}_{\text{CT}}$, $\text{SUVpeak}_{\text{CT}}$, $\text{SUVmax}_{\text{MR}}$, $\text{SUVmean}_{\text{MR}}$ and $\text{SUVpeak}_{\text{MR}}$, respectively. The SUV values were calculated by equation 3. The variable c in the equation was equal to the maximum value in the ROI when calculating SUVmax and equal to the mean value in the ROI when calculating SUVmean. In the case of SUVpeak, c was equal to the average of the maximum pixel and the 8 neighbouring pixels (3x3 pixels).

3.2 ADC

Lesions visible on the ADC map, and visually similar on the PET images of PET/MR, were included in the ADC analysis. ROIs were manually drawn directly on the ADC maps by one person, in accordance with the ROIs on the PET images. As ROIs for ADC measurements differ substantially in the literature, six different shaped ROIs were made in this study to evaluate if different shapes produce different results.

Three distinct configurations were used to draw ROIs in each tumor: all slices covering the lesion, the largest slice (1 slice), and the largest slice with the two adjacent slices (3 slices)(Figure 3.1). For each of these 3 configurations, both the whole area (red and light red area in Figure 3.1) and an inner area (light red area in Figure 3.1) of the tumor were included, producing 6 ROIs for each tumor. The inner area excluded the outermost pixels in each slice, and the uppermost and lowest slice.

The minimum and mean ADC value, ADCmin and ADCmean, in each of the ROIs were calculated.

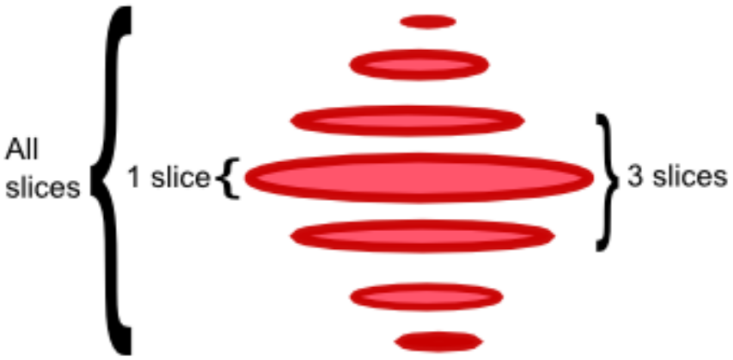

Figure 3.1: ROIs for ADC analysis included all slices, the largest (1 slice) and the largest with the two adjacent slices (3 slices). For each of these 3 configurations, both the whole area of (red and light red) and an inner area (light red) of the slice were included, producing 6 ROIs for each tumor.

3.3 COV

COV for each patient (except for the patient with only one bed position covering pelvis in PET/MR), from both PET/MR and PET/CT, was calculated from the ROI ($r = 15$ mm) in the liver of the patient in the PET image, as in Equation 5.

4 Statistics

The function LinearModel.fit in MATLAB was used to do linear regression on the data. The significance level was set to $P < 0.01$. To test for significant different means, the data was first tested for normality by the Shapiro-Wilk & Shapiro-Francia normality test by the function swtest.m in MATLAB. If the hypothesis of normality was rejected, the Wilcoxon signed rank test (MATLAB, ranksum) was used to test for significant different means, if not, a paired sample t-test (MATLAB, ttest) was used.

Chapter III

Results

1 $\mathbf{SUV_{MR}}$ and $\mathbf{SUV_{CT}}$

The mean SUVmax, SUVmean and SUVpeak of all lesions in each of the 14 patients are compared with the corresponding values measured in a ROI in the aorta and in the liver of the patients in Table 1.1 and in Table 1.2, calculated from PET images from PET/CT and PET/MR, respectively.

None of the SUVmax values for any of the lesions was below 7, which was recommended as a guideline by a nuclear medicine physician, except for one lesion in a PET image from PET/MR, with SUVmax equal to 6.7. This lesion had a SUVmax of 9.7 in PET/CT, and was therefore included.

Patient 74 only had one bed position covering pelvis in the PET/MR examination, hence it was not possible to do the measurements in the aorta and the liver for this patient.

An example of a ROI in the aorta, the liver and a lesion in a PET image from PET/MR is shown in Figure 1.1 .

An example of the same lesion shown in both a PET image obtained from PET/CT and from PET/MR is shown in Figure 1.2.

Table 1.1: Mean SUVmax, SUVmean and SUVpeak from all lesions in each of the 14 patients, and SUVmax, SUVmean and SUVpeak measured in a ROI in the aorta and in the liver of each patient, all calculated in the PET images from PET/CT.

	$SUVmax_{CT}$			$SUVmean_{CT}$			$SUVpeak_{CT}$		
Patient number	Lesions	Aorta	Liver	Lesions	Aorta	Liver	Lesion	Aorta	Liver
59	32.1±0.0	1.6	2.4	19.8±0.0	1.4	1.9	19.3±0.0	1.5	2.2
61	13.0±11.3	1.4	2.6	7.8±6.4	1.3	1.8	9.8±8.2	1.4	2.2
62	25.2±0.0	1.9	2.7	14.4±0.0	1.8	2.1	22.1±0.0	1.8	2.4
65	9.7±0.0	1.8	3.2	5.8±0.0	1.7	2.2	7.2±0.0	1.8	2.8
66	9.0±1.8	2.0	2.9	5.3±1.1	1.8	2.3	5.9±0.7	2.0	2.6
67	13.0±4.2	2.0	2.8	8.0±2.7	1.9	2.2	10.6±4.1	1.8	2.5
68	15.8±5.7	1.8	3.5	9.7±3.6	1.7	2.6	11.3±5.0	1.9	3.1
69	9.1±1.6	1.7	2.8	5.1±0.9	1.5	2.1	6.8±1.4	1.7	2.4
71	10.8±0.0	1.9	2.6	6.4±0.0	1.7	2.0	8.0±0.0	1.8	2.4
72	11.2±3.0	1.3	2.1	6.5±1.7	1.2	1.7	8.8±2.8	1.3	1.9
73	13.5±0.0	1.4	2.6	8.3±0.0	1.4	2.1	9.0±0.0	1.5	2.4
74	10.3±1.8	2.3	3.2	6.4±1.3	2.1	2.4	7.6±1.4	2.2	2.9
75	11.9±1.5	1.9	2.8	7.0±0.9	1.6	2.2	8.6±1.3	1.7	2.6
76	12.3±0.0	1.4	2.2	8.1±0.0	1.3	1.8	11.3±0.0	1.4	2.0

Table 1.2: Mean SUVmax, SUVmean and SUVpeak from all lesions in each of the 14 patients, and SUVmax, SUVmean and SUVpeak measured in a ROI in the aorta and in the liver of each patient, all calculated in the PET images from the PET/MR. Patient 74 only had one bed position covering pelvis, and measurements in the aorta and the liver was not possible.

	$SUVmax_{MR}$			$SUVmean_{MR}$			$SUVpeak_{MR}$		
Patient number	Lesions	Aorta	Liver	Lesions	Aorta	Liver	Lesion	Aorta	Liver
59	41.2±0.0	1.4	2.7	23.8±0.0	1.1	1.9	28.4±0.0	1.3	2.5
61	13.4±10.0	1.0	2.2	8.3±6.7	0.9	1.6	11.3±8.3	1.0	2.1
62	24.5±0.0	1.4	2.3	14.6±0.0	1.2	1.6	20.2±0.0	1.2	2.1
65	6.7±0.0	1.2	2.3	4.0±0.0	1.0	1.6	5.5±0.0	1.1	2.0
66	10.8±1.5	1.3	2.2	6.5±1.2	1.0	1.5	8.2±0.7	1.2	1.9
67	13.6±4.0	1.2	2.7	8.3±2.6	1.1	1.9	12.1±4.0	1.2	2.5
68	17.3±6.3	1.4	2.9	10.5±4.0	1.2	2.3	14.1±6.0	1.3	2.8
69	9.3±3.1	1.7	2.1	5.8±0.4	1.4	1.4	8.3±2.7	1.4	2.0
71	9.7±0.0	0.8	2.2	5.9±0.0	0.7	1.6	8.0±0.0	0.9	2.0
72	13.1±3.4	1.0	1.7	7.1±1.0	0.7	1.1	11.0±2.9	0.9	1.5
73	15.1±0.0	1.1	2.6	9.5±0.0	1.0	1.7	11.4±0.0	1.1	2.2
74	14.4±0.6	-	-	8.7±0.5	-	-	11.3±0.7	-	-
75	11.5±1.9	1.9	2.1	6.7±1.1	1.6	1.7	9.2±1.5	1.7	2.0
76	13.8±0.0	1.5	1.9	8.9±0.0	1.1	1.3	12.7±0.0	1.3	1.7

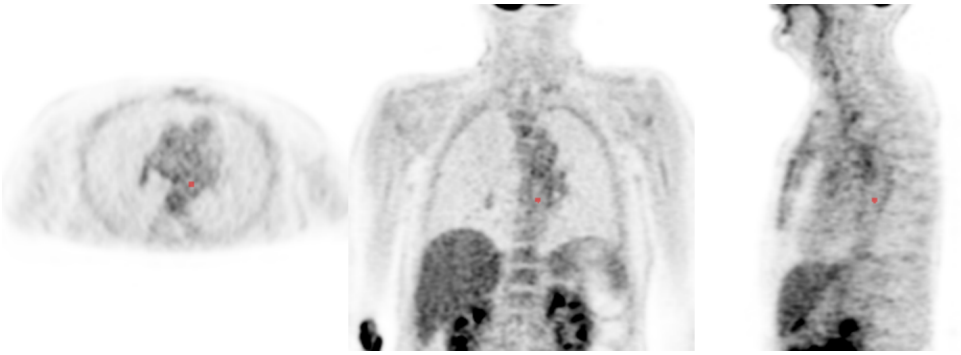

(a)

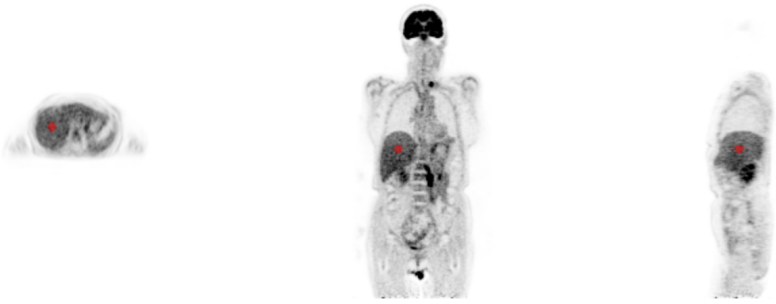

(b)

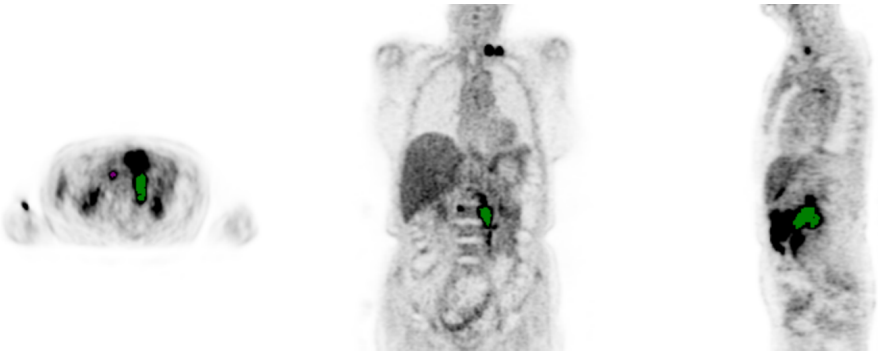

(c)

Figure 1.1: ROIs in a PET image from PET/MR. **(a)** A red ROI in the aorta, **(b)** a red ROI in the liver, **(c)** a green and a purple (only in the axial image) ROI in lesions.

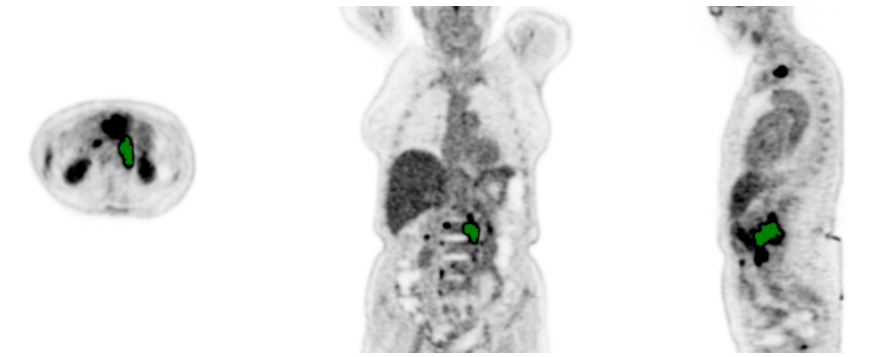

(a)

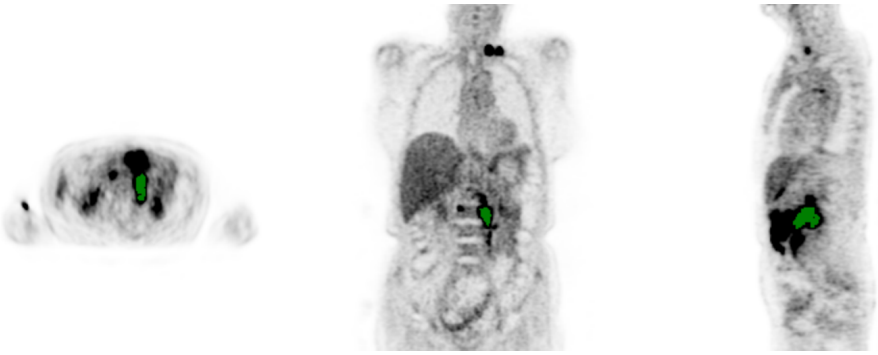

(b)

Figure 1.2: The same lesion (green) in PET images from **(a)** PET/CT and **(b)** PET/MR.

2 SUV_{MR} versus SUV_{CT}

The average SUVmax, SUVmean and SUVpeak of all lesions ($n = 42$) acquired from PET/MR and PET/CT are shown in Table 2.1. SUVmax ($P = 0.19$) and SUVmean ($P = 0.21$) were not found to be significantly different for PET/MR and PET/CT, while SUVpeak ($P < 0.01$) was significantly higher for PET/MR compared to PET/CT.

Table 2.1: The average SUVmax, SUVmean and SUVpeak for PET/MR and PET/CT for all lesions ($n = 42$) in 14 patients.

	SUVmax (mean±std)	SUVmean (mean±std)	SUVpeak (mean±std)
PET/MR	14.1±6.9	8.4±4.2	11.5±5.4
PET/CT	13.0±6.3	7.8±3.8	9.6±4.8
P-value	0.19	0.21	<0.01

There was a strong significant correlation between $\text{SUVmax}_{\text{MR}}$ and $\text{SUVmax}_{\text{CT}}$ ($r = 0.95, P < 0.01$) (Figure 2.1), $\text{SUVmean}_{\text{MR}}$ and $\text{SUVmean}_{\text{CT}}$ ($r = 0.97, P < 0.01$) (Figure 2.2), and $\text{SUVpeak}_{\text{MR}}$ and $\text{SUVpeak}_{\text{CT}}$ ($r = 0.94, P < 0.01$) (Figure 2.3).

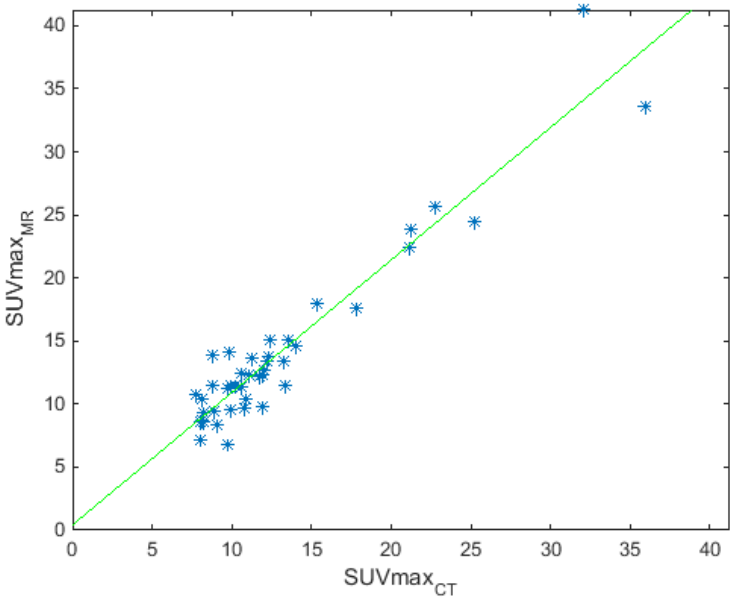

Figure 2.1: The correlation between $\text{SUVmax}_{\text{MR}}$ and $\text{SUVmax}_{\text{CT}}$ ($r = 0.95, P < 0.01$).

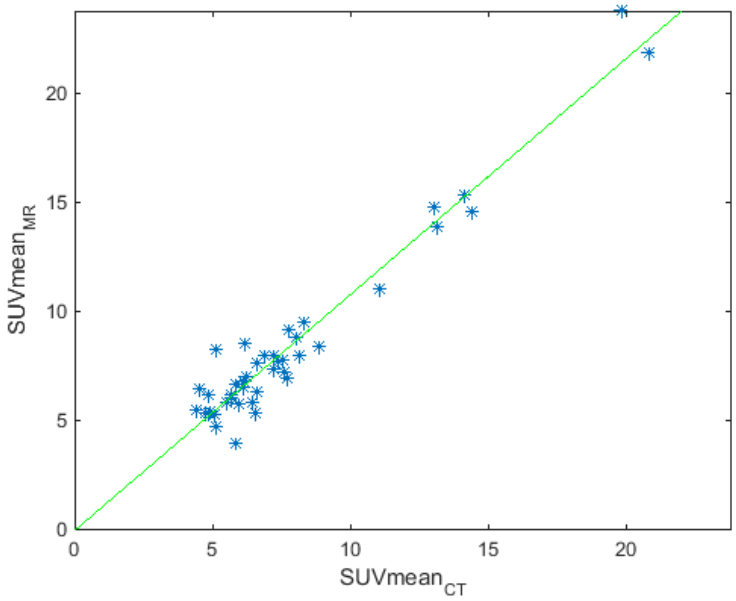

Figure 2.2: The correlation between $\text{SUVmean}_{\text{MR}}$ and $\text{SUVmean}_{\text{CT}}$ ($r = 0.97, P < 0.01$).

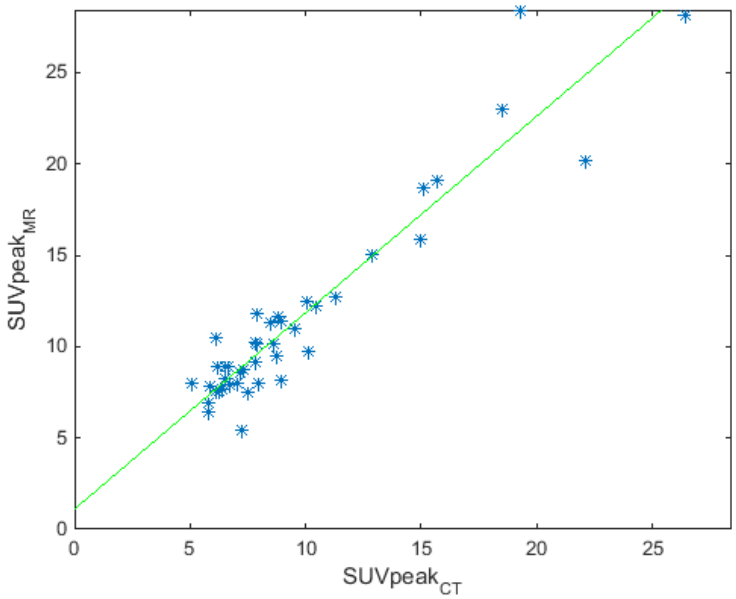

Figure 2.3: The correlation between $\text{SUVpeak}_{\text{MR}}$ and $\text{SUVpeak}_{\text{CT}}$ ($r = 0.94, P < 0.01$).

3 ADC

3.1 ADCmin and ADCmean

The lesions had a decreased intensity compared to the surrounding tissue on the ADC maps, as expected, except for one lesion (patient 69), where the contrast was opposite. ADCmin and ADCmean were highest for this lesion.

The average ADCmin and ADCmean measured in six different shaped ROIs in 7 lesions are shown in Table 3.1. Only 7 of the total 42 lesions were visible and recognizable in the ADC images and included in the ADC analysis.

Table 3.1: Average ADCmin and ADCmean for 7 lesions measured in six different shaped ROIs.

	ADCmin (10^{-3} mm^2/s) (mean±std)	ADCmean (10^{-3} mm^2/s) (mean±std)
Whole area, all slices	305±399	950±482
Whole area, 1 slice	434±501	957±489
Whole area, 3 slices	390±421	944±486
Inner area, all slices	533±298	926±498
Inner area, 1 slice	726±575	924±511
Inner area, 3 slices	644±513	929±500

Examples of manually drawn ROIs in ADC maps are shown in Figure 3.1 a and 3.2 a for patient 72 and patient 75, respectively. The corresponding ROIs in PET images from PET/MR, used for SUV analysis, are shown in Figure 3.1 b and 3.2 b.

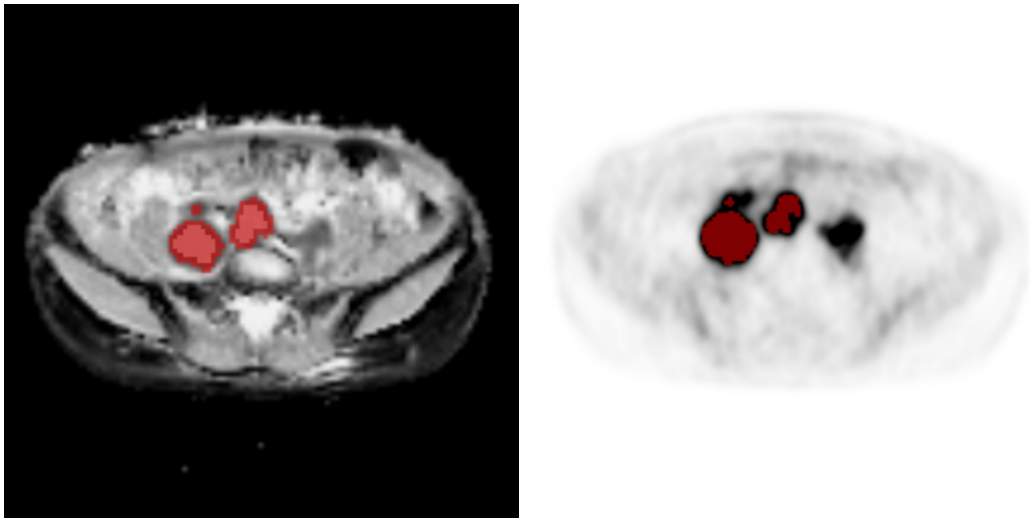

(a) (b)

Figure 3.1: Patient 72, **(a)** ADC map with manually drawn ROI for ADC analysis, with the whole area of the lesion in red and the inner area of the lesion in light red, **(b)** PET image from PET/MR with ROI (red), for SUV analysis.

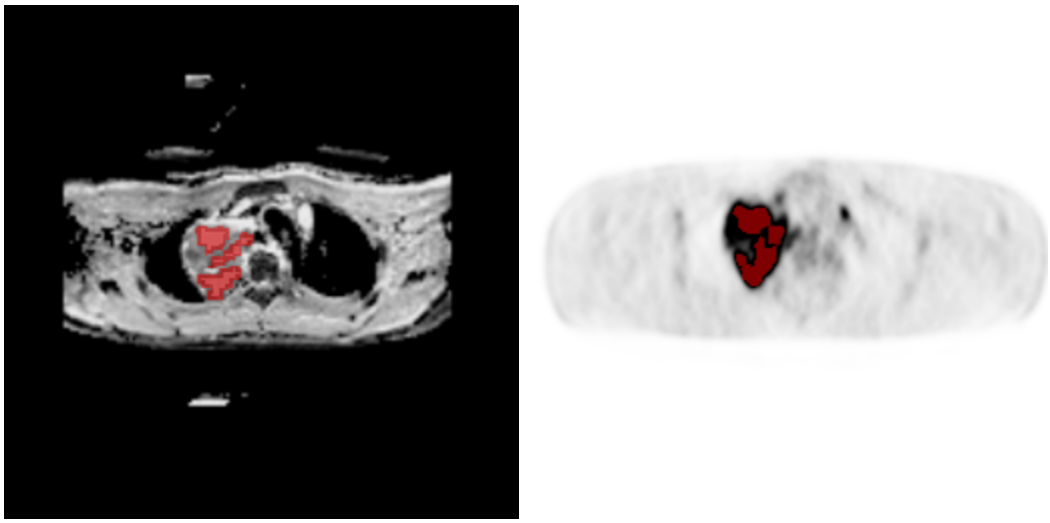

(a) (b)

Figure 3.2: Patient 75, **(a)** ADC map with manually drawn ROI for ADC analysis, with the whole area of the lesion in red and the inner area of the lesion in light red, **(b)** PET image from PET/MR with ROI (red), for SUV analysis.

3.2 ADC versus SUV

There was no significant correlation between ADCmin or ADCmean and SUVmax, SUVmean or SUVpeak in any of the six ROIs, from either PET/MR or PET/CT. An example of the correlations is shown in Figure 3.3, the correlation between ADCmin and $\text{SUVmax}_{\text{MR}}$. All the correlations can be seen in Appendix A (ADC versus SUV).

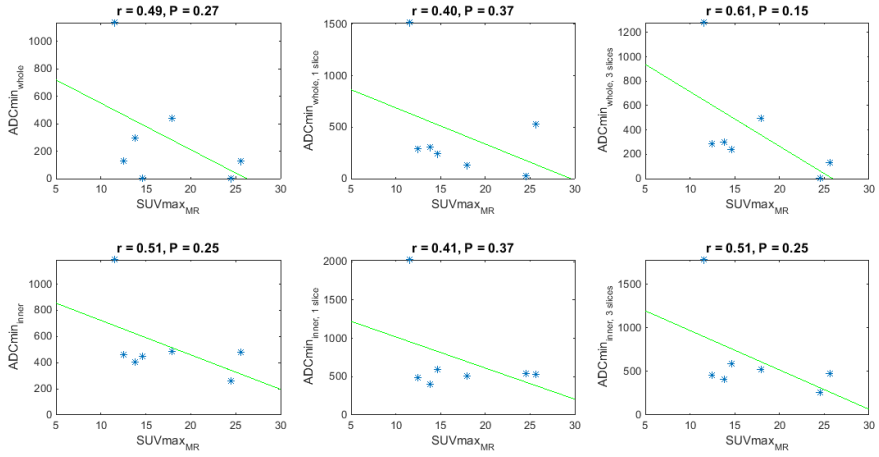

Figure 3.3: No correlation was found between ADCmin and $\text{SUVmax}_{\text{MR}}$ in any of the six different shaped ROIs.

4 COV

The average COV calculated from a ROI in the liver of each of the patients in the PET images of PET/MR and PET/CT, is shown in Table 4.1. COV is significantly higher for PET/MR, compared to PET/CT ($P < 0.01$).

Table 4.1: Average COV calculated from the PET images obtained from PET/MR ($n = 13$) and PET/CT ($n = 14$).

	COV(%) (mean±std)	COV(%) (range)
PET/MR	11.7±2.0	8.3-14.9
PET/CT	9.5±1.2	7.6-12.1
P-value	<0.01	

Chapter IV

Discussion

1 SUV_{MR} and SUV_{CT}

All ROIs of the lesions had a SUVmax above the guideline equal 7, except for one lesion (SUVmax equal to 6.7) in a PET image from PET/MR, which still was included as the SUVmax from PET/CT was above 7. However, no exact lower threshold for malignancy can be set as this depends on several factors.

In the liver, all the SUVmax values were in the interval 2-4 for PET/CT, as recommended, and for PET/MR two values was below 2, but still not very low. SUVmax in the aorta was approximately 1 below the value in the liver for all patients. The uptake of ^{18}F-FDG in healthy tissue seems normal on the basis of these measurements.

2 SUV_{MR} versus SUV_{CT}

The significant correlation found between SUV_{MR} and SUV_{CT} was very strong, and there was no significant difference for SUVmax and SUVmean between PET/MR and PET/CT. These results indicate that SUVmax and SUVmean can be measured from PET/MR as well as from the gold standard method of choice, PET/CT.

SUVpeak, which is not implemented in standardized fashion [4], was significant different between PET/MR and PET/CT. The pixel volume in the PET images from PET/CT is almost 2.3 times larger than in PET/MR, which probably influence the result and cause a significant lower SUVpeak for PET/CT, as a larger volume around the maximum value is covered and causing more smoothing. For SUVmean, this effect is probably not affecting the result due to the larger number of pixels.

Several studies of various cancers have found a strong correlation between SUV from PET/MR and PET/CT, all with a single injection of ^{18}F-FDG and a PET/CT examination followed by a PET/MR examination. A strong

correlation for SUVmax and SUVmean between PET/MR and PET/CT have been found in lesions of NSCLC [27], osseous lesions [21], pulmonary lesions [48], and for SUVmax in neoplastic lesions [46]. Two of the studies did not find a significant difference between PET/MR and PET/CT for SUVmax and SUVmean [27] [48], which is equivalent to our study.

The method chosen for the measurements are slightly different in the various studies. Two of the studies included voxels above 50% of the maximum value in the lesions [48] [21], similar to our approach, except that we used a threshold of 42%, while the two other studies manually placed ROIs covering the whole lesions [46] [27].

SUV obtained from PET/MR was slightly higher than SUV from PET/CT, but as mentioned, there was not a significant difference. Differences in SUV between the two modalities may be induced by the different attenuation correction methods, which use discrete and continuous LACs, respectively [48]. The different arm position in the two scanners (arms down in the PET/MR scanner and arms up in the PET/CT scanner) also cause a great difference in the attenuation correction, as the MR image might be truncated and the arms must be estimated from the PET data in the attenuation map. However, if the arms are not fully recovered in the attenuation map, SUV will be underestimated and this cannot explain the increased SUV for PET/MR. Surface coils that are used in the MR examinations are not accounted for in the attenuation map, which also decrease SUV, potentially with over 16% in tumor lesions [22].

Other technical factors can also influence SUV, such as the difference in spatial resolution of the two scanners, which cause differences in partial volume effects for small objects. A larger pixel size is more likely to cause underestimation of SUV due to smoothing [4], and as the pixel size is larger for PET/CT than PET/MR this may affected our result since SUV_{CT} is lower than SUV_{MR}. Differences in the detectors and geometry of the scanners may also affect SUV.

A biological factor that may influence SUV, is that the amount of tracer trapped in a lesion is increasing with uptake time [48]. However, this effect is reduced for uptake times exceeding 60 minutes and does probably not influenced our measurements as the uptake time for PET/CT is approximately 60 minutes, and longer for PET/MR. Other biological factors, like blood glucose level and respiratory motion may also affect SUV.

Although there are a lot of technical and biological differences between the two examinations that can cause discrepancies in the quantitative measurements, we found no significant difference for SUVmax and SUVmean between PET/MR and PET/CT, and the correlation between them was strong. These results strongly indicate that SUVmax and SUVmean measurements from PET/MR are reliable. Qualitative, visual studies of PET/MR should however be performed before PET/MR can be used in clinic routine for lymphoma patients.

3 ADC

ADC (ADCmin or ADCmean) did not correlate with SUV_{MR} ($SUVmax_{MR}$, $SUVmean_{MR}$ or $SUVpeak_{MR}$), for any of the six shapes of ROIs. The attenuation correction of PET/CT is the gold standard method of choice, and the uptake time for the PET/CT examination was more clinical realistic than for PET/MR, therefore the correlation between ADC and SUV_{CT} ($SUVmax_{CT}$, $SUVmean_{CT}$ or $SUVpeak_{CT}$) was also investigated. Due to the strong correlation between SUV_{MR} and SUV_{CT}, it was not likely that ADC would correlate with SUV_{CT}, and no correlation was found in this case either.

A limitation in this study is the small number of ADC measurements, because only large tumors were visible and possible to recognize in the ADC maps. The results are therefore not reliable.

Another aspect affecting the results is the method for selecting ROIs and how the ROIs for SUV and ADC analysis are related. At a first attempt, we tried to co-register the PET and MR images, in that way the ROIs made in PET images could be copied to the ADC maps and all forty-two lesions could be used. This method would have been optimal and lead to a more accurate comparison between ADC and SUV, however, co-registration is not clinical realistic. The co-registration did not work out very well, as the ROIs did not fit the lesions in the ADC maps. This could probably be due to different contrast in the MR and PET images that were registered to each other. For this reason it was decided to manually draw ROIs directly on the ADC map. Only lesions clearly visible in the ADC map could therefore be used, to get reliable measurements. This method is more clinical realistic, but is very dependent on the person drawing. Individual measurements by several persons should be performed in future studies to avoid individual errors, and hence get a more reliable result.

One of the patients had a high intensity in the lesion compared to the surrounding tissue on the ADC map, unlike the other patients where the contrast was opposite. This lesion had a higher ADCmin and ADCmean compared to the other lesions where ADC was measured. Even if this lesion was excluded, there was no correlation between ADC and SUV for any of the six shapes of ROIs.

The literature reports variable results of the correlation between ADC and SUV in lymphoma patients, and the studies are carried out in different ways regarding the choice of lesions and configurations of ROIs. Only studies including standalone MR scanners and PET/CT or standalone PET scanners have been performed in lymphoma patients, to our knowledge.

In contradiction to our results, Wu et al. found an inverse significant correlation between SUVmax and ADCmean in one study [62], and between SUVmax and ADCmin in another study [64]. The first study included only DL-

BCL patients ($n = 8$), while the second study included both DLBCL ($n = 23$) and FL ($n = 11$) patients. However, no correlation was found between SUVmax and ADCmean in the second study, and when the patients were divided into subgroups, no correlation was found between SUVmax and ADCmin either. The PET/CT examination was performed within 2 days of the MR examination in both studies. The lesions with highest intensity in the PET images were chosen for SUV analysis in both studies. For ADC analysis, up to the five largest lesions were used in the first study, and the largest lesion in the second. Hence, different tumors were used for SUV and ADC analysis in many of patients, in contrast to our study. ROIs were manually placed on the ADC maps, in the five largest cross sections and in each slice of the lesion, respectively. The ADCmean was measured both in the center and periphery of the tumor in the first study, and inverse correlation with SUVmax was found in both cases.

In line with our results, Wu et al. [63] and de Jong et al. [16], did not find any correlation between ADCmean and SUV (SUVmax and SUVmean, and SUVmax, SUVmean and SUVpeak, respectively). Both studies had a homogeneous DLBCL patient group, and 28 and 42 lesions were included, respectively.

Wu et al. included lesions that best matched on the PET/CT and DWI images and the ROIs for ADC measurements were manually placed in the ADC maps on each slice of the tumor. De Jong et al. chose the largest lesion and the lesion with the visually highest uptake of FDG, and the ROIs for ADC measurements were manually placed in the ADC maps in a single transversal slice of the tumors. The same lesions were used for SUV and ADC analysis in both studies, and the PET/CT and MR examinations were performed within 2 days for Wu et al. and within 29 days for de Jong et al.

De Jong et al. performed their study in the same patient group as in one of the studies where Wu et al. found correlation [62], but did not find a correlation. An explanation of this could be the long delay between the two examinations by de Jong. A long delay between the PET and MR examination may give serious alterations in the tumor microstructure, and the probability of correlation between SUV and ADC may decrease.

On the other hand, Wu et al. [63] did have a similar delay between the two examinations as the studies that found correlation, and this cannot explain the discrepancies between the results. Still, the delay between the PET and MR examination may influence the results. However, the studies that found a correlation did not include the same lesions for SUV and ADC analysis for all patients, which could affect the correlation.

In the study by Rakheja et al. [46], (mentioned in the section above, SUV_{MR} *versus* SUV_{CT}), they evaluated the correlation between SUVmax from both PET/MR and PET/CT and ADCmin, not specific for lymphoma pa-

tients, but in neoplastic lesions in general. They found a weak to moderate inverse correlation between SUVmax (from both PET/MR and PET/CT) and ADCmin for nonosseous soft-tissue lesions, and no correlation for osseous lesions. The lesions were manually drawn on the PET images of PET/MR and PET/CT. These ROIs was copied to ADC maps and slightly modified, for ADC analysis. Hence they found correlation between SUV and ADC measured in the same lesions, however, the correlation was found for soft-tissue lesions in general.

Like SUV, ADC is also dependent on several factors, as DWI is sensitive to artifacts, like respiration artifacts [63]. Another limitation, is that diffusion in normal lymph nodes is reduced due to high cellularity of lymph nodes, and diffusion in malignant lymph nodes can be increased due to necrosis and apoptosis, which can make the differentiation between normal and malignant lymph nodes challenging [34]. Diffusion, and hence ADC, can also be influenced by extracellular fibrosis, the shape and size of the intercellular spaces, and other microscopic tissue/tumor organizational characteristics [41]. However, Kwee et al. found that ADC was significant lower in lymphomatous lymph nodes, than in normal lymph nodes [35]. Necrosis and apoptosis can may explain the high intensity in one lesion in this study compared to the surrounding tissue in the ADC map, as mentioned above.

Aggressive lymphomas have an increased glycolysis (which use glucose), mainly due to the overexpression of glucose membrane transporters and a low concentration of glucose-6-phosphatase, as mentioned, and hence an increased uptake of ^{18}F-FDG and an increased SUV. While DWI detects the microscopic changes in water mobility in tumors, even before anatomical changes become visible. As the malignant tissue has an increased cellularity, dense cell membranes, large cell nuclei and reduced extra-cellular space, the water mobility is reduced and the ADC values are decreased [64].

SUV represent the glucose metabolism regardless of the microscopic changes provided by ADC, and opposite, hence SUV and ADC reflects different functional processes. More studies are required to evaluate if SUV is a preferred quantitative measure of malignancy above ADC in lymphoma, or the opposite, or if they are complementary and both providing valuable information in the diagnosis, staging and therapy response of lymphoma. If ADC can replace SUV in assessing therapy response, the radioactive injected dose is not required, which is especially preferable for children and pregnant patients.

4 COV

The mean COV from PET/MR was significantly higher than the mean COV from PET/CT, indicating a worse image quality of the PET images obtained from PET/MR compared to PET/CT.

The different attenuation correction methods for PET/MR and PET/CT, as discussed for SUV, may have a high impact on this result.

The fact that the PET/MR examination is done with a longer uptake time, which is compensated for by an extended acquisition time, may also influence the results. The uptake time should be the same for PET/CT and PET/MR to avoid influence by this factor. Still, this is not feasible as it is unethical to inject the patients with a radioactive dose twice without obtaining any new valuable information. However, since the uptake time for PET/CT was approximately 60 minutes and longer for PET/MR, this factor should not have a high influence, as mentioned.

In our prior study [39], PET images of PET/CT of normal weighted patients (BMI:18.5-24.9 kg/m^2) were considered to be of very good image quality by the nuclear medicine physicians at St. Olavs Hospital. These images had a COV of 9.6±0.7%, which the PET images from PET/CT in this study are comparable to. The PET images from PET/MR, are comparable to those of overweighted patients (BMI $\geq$ 30 kg/m^2) in the prior study, which had a reduced image quality and a mean COV of 11.6±1.5%. In the prior study it was suggested to use an extended acquisition time (180 s) for overweighted patients, to decrease COV. As the acquisition time is already long (300 s) in this case, the probability of motion will be very high with an even longer acquisition time.

Further work should be performed to detect if the image quality of PET images from PET/MR is reduced due to the differences in attenuation correction (especially by the patient's different arm position), the extended uptake and acquisition time or physical properties of the PET/MR scanner (such as APDs, coils etc.). The reconstruction parameters have been optimized at the Biograph mMR scanner at St. Olavs Hospital, so further work to improve image quality could for example include evaluation of acquisition settings, like the acquisition time per bed position which is now based on the European Association of Nuclear Medicine (EANM) procedure guidelines. Visual evaluation of the image quality, with comparison of detected lesions in PET/CT and PET/MR, will also be performed in future studies.

Chapter V

Conclusion

The semi-quantitative measures SUVmax and SUVmean measured from PET/MR and PET/CT in lymphoma patients, strongly correlated and did not differ significantly. According to these results, SUVmax and SUVmean obtained from PET/MR should be reliable, compared to the gold standard PET/CT.

No correlation was found between ADC and SUV. However, the data set was too small to conclude that there is no relationship between ADC and SUV.

COV, a measure of image quality, was found to be increased for the PET images from PET/MR, compared to PET/CT, indicating a reduced PET image quality for PET/MR.

Further work should be performed to determine if PET/MR also is qualitatively comparable to the gold standard for imaging of lymphoma patients, PET/CT. The PET image quality of PET/MR should also be further evaluated to determine the cause of the reduced image quality.

Bibliography

[1] Lymphoma Research Foundation, Hodgkin Lymphoma, 2012. http://www.lymphoma.org/site/pp.asp?c=bkLTKaOQLmK8E&b=6293111. Accessed: 05-22-2014.

[2] Lymphoma Research Foundation, Non-Hodgkin Lymphoma, 2012. http://www.lymphoma.org/site/apps/s/content.asp?c=bkLTKaOQLmK8E&b=6298135&ct=11560717. Accessed: 05-22-2014.

[3] Lars Birger Aasheim, Anna Karlberg, Pål Erik Goa, Asta Håberg, Sveinung Sørhaug, Unn-Merete Fagerli, and Live Eikenes. PET/MR brain imaging: evaluation of clinical UTE-based attenuation correction. *European journal of nuclear medicine and molecular imaging*, pages 1–8, 2015.

[4] M. C. Adams, T. G. Turkington, J. M. Wilson, and T. Z. Wong. A systematic review of the factors affecting accuracy of SUV measurements. *AJR Am J Roentgenol*, 195(2):310–20, 2010. 1546-3141 Adams, Michael C Turkington, Timothy G Wilson, Joshua M Wong, Terence Z Journal Article Research Support, Non-U.S. Gov't Review United States AJR Am J Roentgenol. 2010 Aug;195(2):310-20. doi: 10.2214/AJR.10.4923.

[5] Dale L. Bailey. *Positron emission tomography: basic sciences*. Springer, London, 2005.

[6] I. Bezrukov, F. Mantlik, H. Schmidt, B. Scholkopf, and B. J. Pichler. MR-based PET attenuation correction for PET/MR imaging. *Semin Nucl Med*, 43(1):45–59, 2013. 1558-4623 Bezrukov, Ilja Mantlik, Frederic Schmidt, Holger Scholkopf, Bernhard Pichler, Bernd J Journal Article United States Semin Nucl Med. 2013 Jan;43(1):45-59. doi: 10.1053/j.semnuclmed.2012.08.002.

[7] Ronald Boellaard, Mike J. O'Doherty, Wolfgang A. Weber, Felix M. Mottaghy, Markus N. Lonsdale, Sigrid G. Stroobants, Wim J. G. Oyen, Joerg Kotzerke, Otto S. Hoekstra, Jan Pruim, Paul K. Marsden, Klaus Tatsch, Corneline J. Hoekstra, Eric P. Visser, Bertjan Arends, Fred J. Verzijlbergen, Josee M. Zijlstra, Emile F. I. Comans, Adriaan A. Lammertsma,

Anne M. Paans, Antoon T. Willemsen, Thomas Beyer, Andreas Bockisch, Cornelia Schaefer-Prokop, Dominique Delbeke, Richard P. Baum, Arturo Chiti, and Bernd J. Krause. FDG PET and PET/CT: EANM procedure guidelines for tumour PET imaging: version 1.0. *European Journal of Nuclear Medicine and Molecular Imaging*, 37(1):181–200, 2010. 1297[PII] 19915839[pmid] Eur J Nucl Med Mol Imaging.

[8] Mark A. Brown and Richard C. Semelka. *MRI: basic principles and applications*. Wiley-Liss, Hoboken, N.J., 2003. Previous ed.: New York, N.Y. : Wiley-Liss, 1999. 3rd ed.

[9] Thorsten Buzug. *Computed Tomography: From Photon Statistics to Modern Cone-Beam CT*. Springer Berlin Heidelberg, Berlin, Heidelberg, 2008.

[10] Ignasi Carrio and Pablo Ros. *PET/MRI: Methodology and Clinical Applications*. Springer Berlin Heidelberg, Berlin, Heidelberg, 2014.

[11] Michael E. Casey. Point Spread Function Reconstruction in PET. Report, 2007.

[12] L. Chen, J. Zhang, Y. Chen, W. Wang, X. Zhou, X. Yan, and J. Wang. Relationship between apparent diffusion coefficient and tumour cellularity in lung cancer. *PLoS One*, 9(6):e99865, 2014. 1932-6203 Chen, Lihua Zhang, Jiuquan Chen, Yongfeng Wang, Wenwei Zhou, Xiangdong Yan, Xiaochu Wang, Jian Journal Article United States PLoS One. 2014 Jun 11;9(6):e99865. doi: 10.1371/journal.pone.0099865. eCollection 2014.

[13] Y. Chen, J. Zhong, H. Wu, and N. Chen. The clinical application of whole-body diffusion-weighted imaging in the early assessment of chemotherapeutic effects in lymphoma: the initial experience. *Magn Reson Imaging*, 30(2):165–70, 2012. 1873-5894 Chen, Yunbin Zhong, Jing Wu, Hui Chen, Ningbin Journal Article Netherlands Magn Reson Imaging. 2012 Feb;30(2):165-70. doi: 10.1016/j.mri.2011.09.019. Epub 2011 Nov 30.

[14] Simon R. Cherry, Magnus Dahlbom, and Michael E. Phelps. *PET: physics, instrumentation, and scanners*. New York Springer, 2006.

[15] Mark S. Cohen. Echo-planar imaging (EPI) and functional MRI. `http://www.brainmapping.org/MarkCohen/Papers/EPI-fMRI.html`. Accessed: 06-10-2015.

[16] A. de Jong, T. C. Kwee, J. M. de Klerk, J. A. Adam, B. de Keizer, R. Fijnheer, M. J. Kersten, I. Ludwig, Y. W. Jauw, J. M. Zijlstra, I. C. Pieters-Van den Bos, J. Stoker, O. S. Hoekstra, and R. A. Nievelstein. Relationship between pretreatment FDG-PET and diffusion-weighted MRI

biomarkers in diffuse large B-cell lymphoma. *Am J Nucl Med Mol Imaging*, 4(3):231–8, 2014. 2160-8407 de Jong, Antoinette Kwee, Thomas C de Klerk, John M H Adam, Judit A de Keizer, Bart Fijnheer, Rob Kersten, Marie Jose Ludwig, Inge Jauw, Yvonne W S Zijlstra, Josee M Pieters-Van den Bos, Indra C Stoker, Jaap Hoekstra, Otto S Nievelstein, Rutger A J Journal Article United States Am J Nucl Med Mol Imaging. 2014 Apr 25;4(3):231-8. eCollection 2014.

[17] K. De Paepe, C. Bevernage, F. De Keyzer, P. Wolter, O. Gheysens, A. Janssens, R. Oyen, G. Verhoef, and V. Vandecaveye. Whole-body diffusion-weighted magnetic resonance imaging at 3 Tesla for early assessment of treatment response in non-Hodgkin lymphoma: a pilot study. *Cancer Imaging*, 13:53–62, 2013. 1470-7330 De Paepe, Katja Bevernage, Charlotte De Keyzer, Frederik Wolter, Pascal Gheysens, Olivier Janssens, Ann Oyen, Raymond Verhoef, Gregor Vandecaveye, Vincent Journal Article England Cancer Imaging. 2013 Mar 5;13:53-62. doi: 10.1102/1470-7330.2013.0006.

[18] J. A. Disselhorst, I. Bezrukov, A. Kolb, C. Parl, and B. J. Pichler. Principles of PET/MR imaging. *J Nucl Med*, 55(Supplement 2):2s–10s, 2014. 1535-5667 Disselhorst, Jonathan A Bezrukov, Ilja Kolb, Armin Parl, Christoph Pichler, Bernd J Journal article J Nucl Med. 2014 May 12;55(Supplement 2):2S-10S.

[19] A. Drzezga, M. Souvatzoglou, M. Eiber, A. J. Beer, S. Furst, A. Martinez-Moller, S. G. Nekolla, S. Ziegler, C. Ganter, E. J. Rummeny, and M. Schwaiger. First clinical experience with integrated whole-body PET/MR: comparison to PET/CT in patients with oncologic diagnoses. *J Nucl Med*, 53(6):845–55, 2012. 1535-5667 Drzezga, Alexander Souvatzoglou, Michael Eiber, Matthias Beer, Ambros J Furst, Sebastian Martinez-Moller, Axel Nekolla, Stephan G Ziegler, Sibylle Ganter, Carl Rummeny, Ernst J Schwaiger, Markus Comparative Study Journal Article Research Support, Non-U.S. Gov't United States J Nucl Med. 2012 Jun;53(6):845-55. doi: 10.2967/jnumed.111.098608. Epub 2012 Apr 25.

[20] Maria M. D'Souza, Abhinav Jaimini, Abhishek Bansal, Madhavi Tripathi, Rajnish Sharma, Anupam Mondal, and Rajendra Prashad Tripathi. FDG-PET/CT in lymphoma. *The Indian Journal of Radiology & Imaging*, 23(4):354–365, 2013. IJRI-23-354[PII] 24604942[pmid] Indian J Radiol Imaging.

[21] M. Eiber, T. Takei, M. Souvatzoglou, M. E. Mayerhoefer, S. Furst, F. C. Gaertner, D. J. Loeffelbein, E. J. Rummeny, S. I. Ziegler, M. Schwaiger, and A. J. Beer. Performance of whole-body integrated 18F-FDG PET/MR

in comparison to PET/CT for evaluation of malignant bone lesions. *J Nucl Med*, 55(2):191–7, 2014. 1535-5667 Eiber, Matthias Takei, Toshiki Souvatzoglou, Michael Mayerhoefer, Marius E Furst, Sebastian Gaertner, Florian C Loeffelbein, Denys J Rummeny, Ernst J Ziegler, Sibylle I Schwaiger, Markus Beer, Ambros J Comparative Study Journal Article Research Support, Non-U.S. Gov't United States J Nucl Med. 2014 Feb;55(2):191-7. doi: 10.2967/jnumed.113.123646. Epub 2013 Dec 5.

[22] S. Fürst, M. Souvatzoglou, A. Martinez-Möller, M. Schwaiger, S. G. Nekolla, and S. I. Ziegler. Impact of flexible body surface coil and patient table on PET quantification and image quality in integrated PET/MR. *Nuklearmedizin*, 53(3):79–87, 2014.

[23] E. Mark Haacke. *Magnetic resonance imaging: physical principles and sequence design*. Wiley-Liss, New York, 1999.

[24] HJ Harms, AA Lammertsma, M Lubberink, P Knaapen, and S De Haan. Quantitative myocardial blood flow imaging using PET/CT. 2010.

[25] Chris Hatton, Graham Collins, and John Sweetenham. *Fast Facts : Lymphoma*. Health Press Limited, Abingdon, Oxford, GBR, 2008.

[26] L. Heacock, J. Weissbrot, R. Raad, N. Campbell, K. P. Friedman, F. Ponzo, and H. Chandarana. PET/MRI for the evaluation of patients with lymphoma: initial observations. *AJR Am J Roentgenol*, 204(4):842–8, 2015. 1546-3141 Heacock, Laura Weissbrot, Joseph Raad, Roy Campbell, Naomi Friedman, Kent P Ponzo, Fabio Chandarana, Hersh Comparative Study Journal Article United States AJR Am J Roentgenol. 2015 Apr;204(4):842-8. doi: 10.2214/AJR.14.13181.

[27] P. Heusch, C. Buchbender, J. Kohler, F. Nensa, T. Gauler, B. Gomez, H. Reis, G. Stamatis, H. Kuhl, V. Hartung, and T. A. Heusner. Thoracic staging in lung cancer: prospective comparison of 18F-FDG PET/MR imaging and 18F-FDG PET/CT. *J Nucl Med*, 55(3):373–8, 2014. 1535-5667 Heusch, Philipp Buchbender, Christian Kohler, Jens Nensa, Felix Gauler, Thomas Gomez, Benedikt Reis, Henning Stamatis, Georgios Kuhl, Hilmar Hartung, Verena Heusner, Till A Clinical Trial Journal Article United States J Nucl Med. 2014 Mar;55(3):373-8. doi: 10.2967/jnumed.113.129825. Epub 2014 Feb 6.

[28] F. W. Hirsch, B. Sattler, I. Sorge, L. Kurch, A. Viehweger, L. Ritter, P. Werner, T. Jochimsen, H. Barthel, U. Bierbach, H. Till, O. Sabri, and R. Kluge. PET/MR in children. Initial clinical experience in paediatric oncology using an integrated PET/MR scanner. *Pediatr Radiol*, 43(7):860–75, 2013. 1432-1998 Hirsch, Franz Wolfgang Sattler, Bernhard Sorge, Ina

Kurch, Lars Viehweger, Adrian Ritter, Lutz Werner, Peter Jochimsen, Thies Barthel, Henryk Bierbach, Uta Till, Holger Sabri, Osama Kluge, Regine Journal Article Germany Pediatr Radiol. 2013 Jul;43(7):860-75. doi: 10.1007/s00247-012-2570-4. Epub 2013 Jan 11.

[29] M. Hofmann, B. Pichler, B. Scholkopf, and T. Beyer. Towards quantitative PET/MRI: a review of MR-based attenuation correction techniques. *Eur J Nucl Med Mol Imaging*, 36 Suppl 1:S93–104, 2009. 1619-7089 Hofmann, Matthias Pichler, Bernd Scholkopf, Bernhard Beyer, Thomas Journal Article Review Germany Eur J Nucl Med Mol Imaging. 2009 Mar;36 Suppl 1:S93-104. doi: 10.1007/s00259-008-1007-7.

[30] Harald Holte, Arne Kolstad, Bjørn Østenstad, Øystein Fluge, Alexander Fosså, Eldrid Liljedal, Grete Herzog, Gro Haugen, and Jan Delabie. Nasjonale handlingsprogrammet med retningslinjer for diagnostikk behandling og oppfølging av maligne lymfomer. Report, 2012.

[31] M. Hutchings. PET imaging in lymphoma. *Expert Rev Hematol*, 2(3):261–76, 2009. 1747-4094 Hutchings, Martin Journal Article Review England Expert Rev Hematol. 2009 Jun;2(3):261-76. doi: 10.1586/ehm.09.21.

[32] Heidi Johansen-Berg and Timothy E. J. Behrens. *Diffusion MRI: from quantitative measurement to in vivo neuroanatomy*. Academic Press, Amsterdam, 2014. Includes index. 2nd ed.

[33] Paul E. Kinahan and James W. Fletcher. PET/CT standardized uptake values (SUVs) in clinical practice and assessing response to therapy. *Seminars in ultrasound, CT, and MR*, 31(6):496–505, 2010. 21147377[pmid] Semin Ultrasound CT MR.

[34] T. C. Kwee, T. Takahara, R. Ochiai, D. M. Koh, Y. Ohno, K. Nakanishi, T. Niwa, T. L. Chenevert, P. R. Luijten, and A. Alavi. Complementary roles of whole-body diffusion-weighted MRI and 18F-FDG PET: the state of the art and potential applications. *J Nucl Med*, 51(10):1549–58, 2010. 1535-5667 Kwee, Thomas C Takahara, Taro Ochiai, Reiji Koh, Dow-Mu Ohno, Yoshiharu Nakanishi, Katsuyuki Niwa, Tetsu Chenevert, Thomas L Luijten, Peter R Alavi, Abass Journal Article Review United States J Nucl Med. 2010 Oct;51(10):1549-58. doi: 10.2967/jnumed.109.073908. Epub 2010 Sep 16.

[35] ThomasC Kwee, Inge Ludwig, CunoS Uiterwaal, HenrietteM E. Quarles van Ufford, MalouA Vermoolen, Rob Fijnheer, MarcB Bierings, and RutgerA J. Nievelstein. ADC measurements in the evaluation of lymph

nodes in patients with non-Hodgkin lymphoma: feasibility study. *Magnetic Resonance Materials in Physics, Biology and Medicine*, 24(1):1–8, 2011.

[36] A. Nagaki, M. Onoguchi, and N. Matsutomo. Patient weight-based acquisition protocols to optimize (18)F-FDG PET/CT image quality. *J Nucl Med Technol*, 39(2):72–6, 2011. 1535-5675 Nagaki, Akio Onoguchi, Masahisa Matsutomo, Norikazu Journal Article United States J Nucl Med Technol. 2011 Jun;39(2):72-6. doi: 10.2967/jnmt.110.081661. Epub 2011 May 12.

[37] Cancer Registry of Norway. *Cancer in Norway 2012 - Cancer incidence, mortality, survival and prevalence in Norway.* Oslo: Cancer Registry of Norway, Oslo, 2014.

[38] Y. Ohno, H. Koyama, T. Yoshikawa, K. Matsumoto, N. Aoyama, Y. Onishi, and K. Sugimura. Diffusion-weighted MRI versus 18F-FDG PET/CT: performance as predictors of tumor treatment response and patient survival in patients with non-small cell lung cancer receiving chemoradiotherapy. *AJR Am J Roentgenol*, 198(1):75–82, 2012. 1546-3141 Ohno, Yoshiharu Koyama, Hisanobu Yoshikawa, Takeshi Matsumoto, Keiko Aoyama, Nobukazu Onishi, Yumiko Sugimura, Kazuro Comparative Study Journal Article Research Support, Non-U.S. Gov't United States AJR Am J Roentgenol. 2012 Jan;198(1):75-82. doi: 10.2214/AJR.11.6525.

[39] S. K. Olsen. *Optimization of PET image quality in 18F-FDG PET/CT.* Thesis, 2014.

[40] Medhat M. Osman, Razi Muzaffar, M. Erkan Altinyay, and Cyrus Teymouri. FDG dose extravasations in PET/CT: Frequency and impact on SUV measurements. *Frontiers in Oncology*, 1:41, 2011. 22655246[pmid] Front Oncol.

[41] A. R. Padhani, G. Liu, D. M. Koh, T. L. Chenevert, H. C. Thoeny, T. Takahara, A. Dzik-Jurasz, B. D. Ross, M. Van Cauteren, D. Collins, D. A. Hammoud, G. J. Rustin, B. Taouli, and P. L. Choyke. Diffusion-weighted magnetic resonance imaging as a cancer biomarker: consensus and recommendations. *Neoplasia*, 11(2):102–25, 2009. 1476-5586 Padhani, Anwar R Liu, Guoying Koh, Dow Mu Chenevert, Thomas L Thoeny, Harriet C Takahara, Taro Dzik-Jurasz, Andrew Ross, Brian D Van Cauteren, Marc Collins, David Hammoud, Dima A Rustin, Gordon J S Taouli, Bachir Choyke, Peter L Consensus Development Conference, NIH Journal Article Canada Neoplasia. 2009 Feb;11(2):102-25.

[42] Patrick Peller, Rathan Subramaniam, and Ali Guermazi. *PET-CT and PET-MRI in Oncology: A Practical Guide*. Springer Berlin Heidelberg, Berlin, Heidelberg, 2012.

[43] I. Platzek, B. Beuthien-Baumann, J. Langner, M. Popp, G. Schramm, R. Ordemann, M. Laniado, J. Kotzerke, and J. van den Hoff. PET/MR for therapy response evaluation in malignant lymphoma: initial experience. *Magma*, 26(1):49–55, 2013. 1352-8661 Platzek, Ivan Beuthien-Baumann, Bettina Langner, Jens Popp, Manuel Schramm, Georg Ordemann, Rainer Laniado, Michael Kotzerke, Jorg van den Hoff, Jorg Journal Article Germany MAGMA. 2013 Feb;26(1):49-55. doi: 10.1007/s10334-012-0342-7. Epub 2012 Sep 16.

[44] S. Punwani, S. A. Taylor, Z. Z. Saad, A. Bainbridge, A. Groves, S. Daw, A. Shankar, S. Halligan, and P. D. Humphries. Diffusion-weighted MRI of lymphoma: prognostic utility and implications for PET/MRI? *Eur J Nucl Med Mol Imaging*, 40(3):373–85, 2013. 1619-7089 Punwani, Shonit Taylor, Stuart A Saad, Ziauddin Z Bainbridge, Alan Groves, Ashley Daw, Stephen Shankar, Ananth Halligan, Steve Humphries, Paul D Journal Article Research Support, Non-U.S. Gov't Germany Eur J Nucl Med Mol Imaging. 2013 Feb;40(3):373-85. doi: 10.1007/s00259-012-2293-7. Epub 2012 Nov 30.

[45] H. H. Quick. Integrated PET/MR. *J Magn Reson Imaging*, 39(2):243–58, 2014. 1522-2586 Quick, Harald H Journal Article Research Support, Non-U.S. Gov't Review United States J Magn Reson Imaging. 2014 Feb;39(2):243-58. doi: 10.1002/jmri.24523. Epub 2013 Dec 12.

[46] R. Rakheja, H. Chandarana, L. DeMello, K. Jackson, C. Geppert, D. Faul, C. Glielmi, and K. P. Friedman. Correlation between standardized uptake value and apparent diffusion coefficient of neoplastic lesions evaluated with whole-body simultaneous hybrid PET/MRI. *AJR Am J Roentgenol*, 201(5):1115–9, 2013. 1546-3141 Rakheja, Rajan Chandarana, Hersh DeMello, Linda Jackson, Kimberly Geppert, Christian Faul, David Glielmi, Christopher Friedman, Kent P Journal Article United States AJR Am J Roentgenol. 2013 Nov;201(5):1115-9. doi: 10.2214/AJR.13.11304.

[47] E. Rapisarda, V. Bettinardi, K. Thielemans, and M. C. Gilardi. Image-based point spread function implementation in a fully 3D OSEM reconstruction algorithm for PET. *Phys Med Biol*, 55(14):4131–51, 2010. 1361-6560 Rapisarda, E Bettinardi, V Thielemans, K Gilardi, M C Journal Article Validation Studies England Phys Med Biol. 2010 Jul 21;55(14):4131-51. doi: 10.1088/0031-9155/55/14/012. Epub 2010 Jul 5.

[48] I. Rauscher, M. Eiber, S. Furst, M. Souvatzoglou, S. G. Nekolla, S. I. Ziegler, E. J. Rummeny, M. Schwaiger, and A. J. Beer. PET/MR imaging in the detection and characterization of pulmonary lesions: technical and diagnostic evaluation in comparison to PET/CT. *J Nucl Med*, 55(5):724–9, 2014. 1535-5667 Rauscher, Isabel Eiber, Matthias Furst, Sebastian Souvatzoglou, Michael Nekolla, Stephan G Ziegler, Sibylle I Rummeny, Ernst J Schwaiger, Markus Beer, Ambros J Comparative Study Journal Article United States J Nucl Med. 2014 May;55(5):724-9. doi: 10.2967/jnumed.113.129247. Epub 2014 Mar 20.

[49] D. Rizzo. *Fundamentals of Anatomy and Physiology*. Cencage Learning, 2010.

[50] Emilie Roncali and Simon R. Cherry. Application of silicon photomultipliers to positron emission tomography. *Annals of Biomedical Engineering*, 39(4):1358–1377, 2011. 266[PII] 21321792[pmid] Ann Biomed Eng.

[51] Heinz-Peter W. Schlemmer, Bernd J. Pichler, Matthias Schmand, Ziad Burbar, Christian Michel, Ralf Ladebeck, Kirstin Jattke, David Townsend, Claude Nahmias, Pradeep K. Jacob, Wolf-Dieter Heiss, and Claus D. Claussen. Simultaneous MR/PET imaging of the human brain: Feasibility study. *Radiology*, 248(3):1028–1035, 2008.

[52] Franz Schmitt, Robert Turner, M. K. Stehling, and Peter A. Bandettini. *Echo-planar imaging: theory, technique and application*. Springer, Erlangen, 1998.

[53] P. Seam, M. E. Juweid, and B. D. Cheson. The role of FDG-PET scans in patients with lymphoma. *Blood*, 110(10):3507–16, 2007. Seam, Pamela Juweid, Malik E Cheson, Bruce D Evaluation Studies Journal Article Review United States Blood. 2007 Nov 15;110(10):3507-16. Epub 2007 Aug 20.

[54] Euclid Seeram. *Computed tomography: physical principles, clinical applications, and quality control*. Elsevier Health Sciences, 2013.

[55] I. L. Shih, R. F. Yen, C. A. Chen, B. B. Chen, S. Y. Wei, W. C. Chang, B. C. Sheu, W. F. Cheng, Y. H. Tseng, X. J. Chen, C. H. Chen, L. H. Wei, Y. C. Chiang, P. L. Torng, M. L. Yen, and T. T. Shih. Standardized uptake value and apparent diffusion coefficient of endometrial cancer evaluated with integrated whole-body PET/MR: Correlation with pathological prognostic factors. *J Magn Reson Imaging*, 2015. 1522-2586 Shih, I-Lun Yen, Ruoh-Fang Chen, Chi-An Chen, Bang-Bin Wei, Shwu-Yuan Chang, Wen-Chun Sheu, Bor-Ching Cheng, Wen-Fang Tseng, Yao-Hui Chen, Xin-Jia Chen, Chi-Hau Wei, Lin-Hung Chiang, Ying-Cheng Torng,

Pao-Ling Yen, Men-Luh Shih, Tiffany Ting-Fang Journal article J Magn Reson Imaging. 2015 Apr 27. doi: 10.1002/jmri.24932.

[56] M. J. Siegel, C. E. Jokerst, D. Rajderkar, C. F. Hildebolt, S. Goyal, F. Dehdashti, N. Wagner Johnston, and B. A. Siegel. Diffusion-weighted MRI for staging and evaluation of response in diffuse large B-cell lymphoma: a pilot study. *NMR Biomed*, 27(6):681–91, 2014. 1099-1492 Siegel, Marilyn J Jokerst, Clint E Rajderkar, Dhana Hildebolt, Charles F Goyal, Sagun Dehdashti, Farrokh Wagner Johnston, Nina Siegel, Barry A P30 CA091842/CA/NCI NIH HHS/United States UL1 TR000448/TR/NCATS NIH HHS/United States Journal Article Research Support, N.I.H., Extramural Research Support, Non-U.S. Gov't England NMR Biomed. 2014 Jun;27(6):681-91. doi: 10.1002/nbm.3105. Epub 2014 Apr 3.

[57] Virginia Ch Spanoudaki and Craig S. Levin. Photo-detectors for time of flight positron emission tomography (ToF-PET). *Sensors (Basel, Switzerland)*, 10(11):10484–10505, 2010. sensors-10-10484-v3[PII] 22163482[pmid] Sensors (Basel).

[58] DavidW Townsend. *Basic Science of PET and PET/CT*, book section 1, pages 1–16. Springer London, 2006.

[59] GustavK von Schulthess and Heinz-PeterW Schlemmer. A look ahead: PET/MR versus PET/CT. *European Journal of Nuclear Medicine and Molecular Imaging*, 36(1):3–9, 2009.

[60] G. Wagenknecht, H. J. Kaiser, F. M. Mottaghy, and H. Herzog. MRI for attenuation correction in PET: methods and challenges. *Magma*, 26(1):99–113, 2013. 1352-8661 Wagenknecht, Gudrun Kaiser, Hans-Jurgen Mottaghy, Felix M Herzog, Hans Journal Article Review Germany MAGMA. 2013 Feb;26(1):99-113. doi: 10.1007/s10334-012-0353-4. Epub 2012 Nov 21.

[61] R. L. Wahl, H. Jacene, Y. Kasamon, and M. A. Lodge. From RECIST to PERCIST: Evolving considerations for PET response criteria in solid tumors. *J Nucl Med*, 50 Suppl 1:122s–50s, 2009. Wahl, Richard L Jacene, Heather Kasamon, Yvette Lodge, Martin A 3 P30 CA006973-43S2/CA/NCI NIH HHS/United States P30 CA006973-43S2/CA/NCI NIH HHS/United States Journal Article Research Support, N.I.H., Extramural Review United States J Nucl Med. 2009 May;50 Suppl 1:122S-50S. doi: 10.2967/jnumed.108.057307.

[62] X. Wu, P. L. Kellokumpu-Lehtinen, H. Pertovaara, P. Korkola, S. Soimakallio, H. Eskola, and P. Dastidar. Diffusion-weighted MRI in

early chemotherapy response evaluation of patients with diffuse large B-cell lymphoma–a pilot study: comparison with 2-deoxy-2-fluoro- d-glucose-positron emission tomography/computed tomography. *NMR Biomed*, 24(10):1181–90, 2011. 1099-1492 Wu, Xingchen Kellokumpu-Lehtinen, Pirkko-Liisa Pertovaara, Hannu Korkola, Pasi Soimakallio, Seppo Eskola, Hannu Dastidar, Prasun Clinical Trial Comparative Study Journal Article Research Support, Non-U.S. Gov't England NMR Biomed. 2011 Dec;24(10):1181-90. doi: 10.1002/nbm.1689. Epub 2011 Mar 8.

[63] X. Wu, P. Korkola, H. Pertovaara, H. Eskola, R. Jarvenpaa, and P. L. Kellokumpu-Lehtinen. No correlation between glucose metabolism and apparent diffusion coefficient in diffuse large B-cell lymphoma: a PET/CT and DW-MRI study. *Eur J Radiol*, 79(2):e117–21, 2011. 1872-7727 Wu, Xingchen Korkola, Pasi Pertovaara, Hannu Eskola, Hannu Jarvenpaa, Ritva Kellokumpu-Lehtinen, Pirkko-Liisa Journal Article Research Support, Non-U.S. Gov't Ireland Eur J Radiol. 2011 Aug;79(2):e117-21. doi: 10.1016/j.ejrad.2011.04.062. Epub 2011 May 18.

[64] X. Wu, H. Pertovaara, P. Korkola, P. Dastidar, R. Jarvenpaa, H. Eskola, and P. L. Kellokumpu-Lehtinen. Correlations between functional imaging markers derived from PET/CT and diffusion-weighted MRI in diffuse large b-cell lymphoma and follicular lymphoma. *PLoS One*, 9(1):e84999, 2014. 1932-6203 Wu, Xingchen Pertovaara, Hannu Korkola, Pasi Dastidar, Prasun Jarvenpaa, Ritva Eskola, Hannu Kellokumpu-Lehtinen, Pirkko-Liisa Journal Article Research Support, Non-U.S. Gov't United States PLoS One. 2014 Jan 15;9(1):e84999. doi: 10.1371/journal.pone.0084999. eCollection 2014.

Appendices

Appendix A

ADC versus SUV

No correlation was found between ADCmin or ADCmean and SUVmax, SUVmean or SUVpeak from PET/MR, in any of the six different shaped ROIs, as seen in Figure A.1-A.6. No correlation was either found between ADCmin or ADCmean and SUVmax, SUVmean or SUVpeak from PET/CT, in any of the six different shaped ROIs, as seen in Figure A.7-A.12.

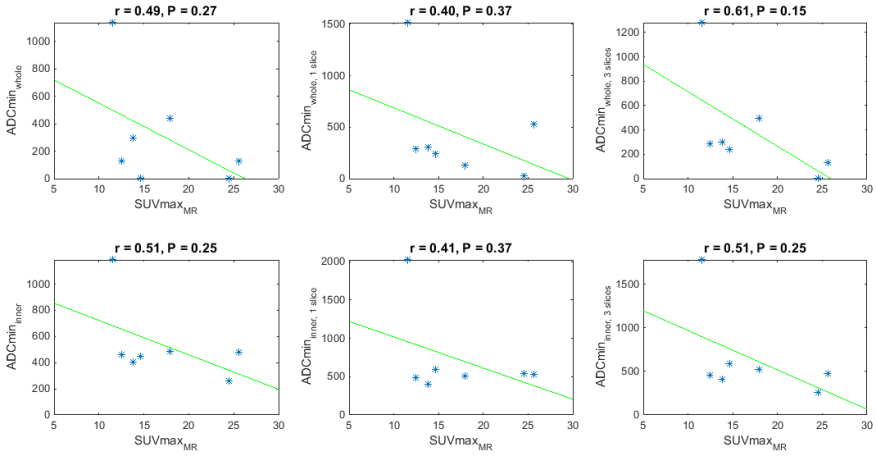

Figure A.1: No correlation was found between ADCmin and $\text{SUVmax}_{\text{MR}}$ in any of the six different shaped ROIs.

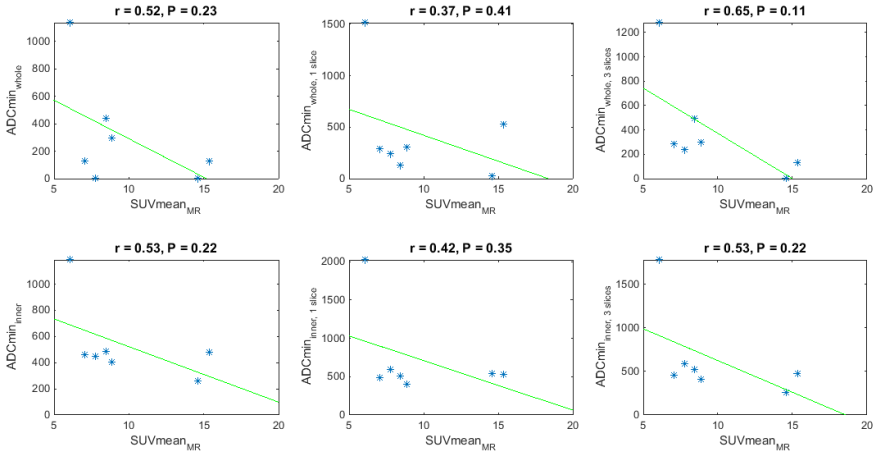

Figure A.2: No correlation was found between ADCmin and $\text{SUVmean}_{\text{MR}}$ in any of the six different shaped ROIs.

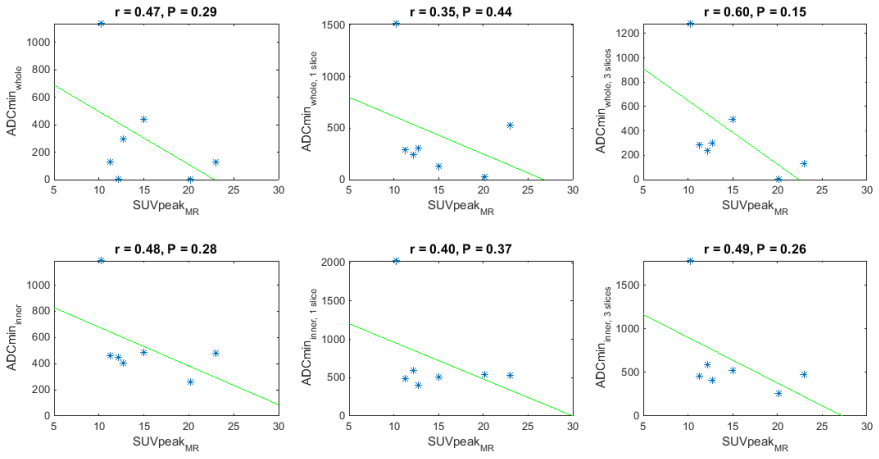

Figure A.3: No correlation was found between ADCmin and $\text{SUVpeak}_{\text{MR}}$ in any of the six different shaped ROIs.

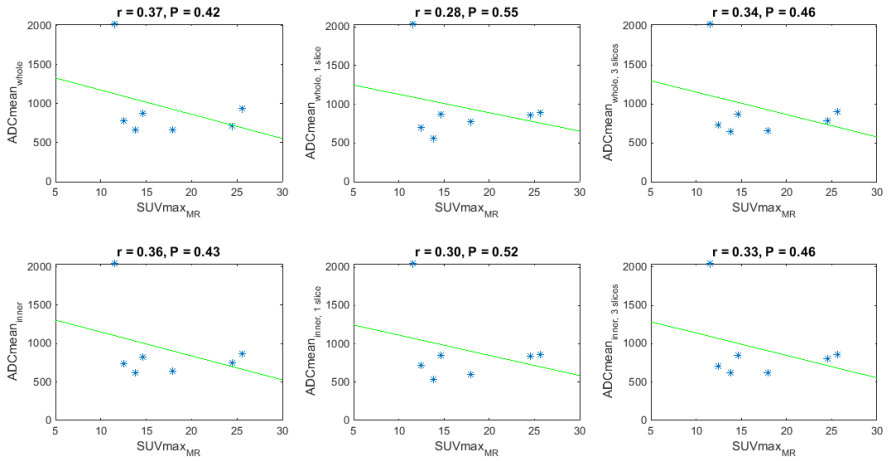

Figure A.4: No correlation was found between ADCmean and $\text{SUVmax}_{\text{MR}}$ in any of the six different shaped ROIs.

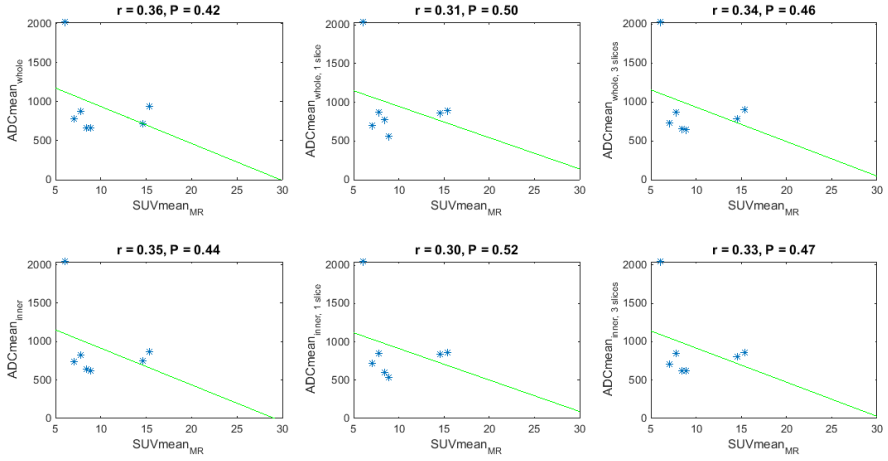

Figure A.5: No correlation was found between ADCmean and $\text{SUVmean}_{\text{MR}}$ in any of the six different shaped ROIs.

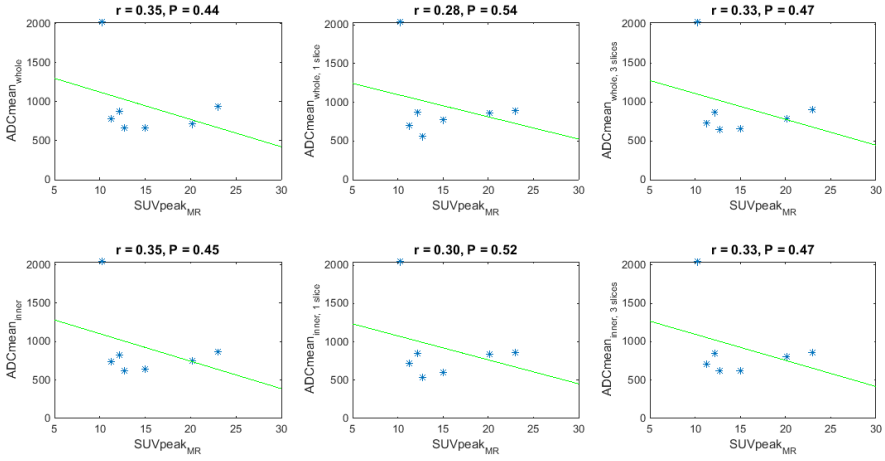

Figure A.6: No correlation was found between ADCmean and $\text{SUVpeak}_{\text{MR}}$ in any of the six different shaped ROIs.

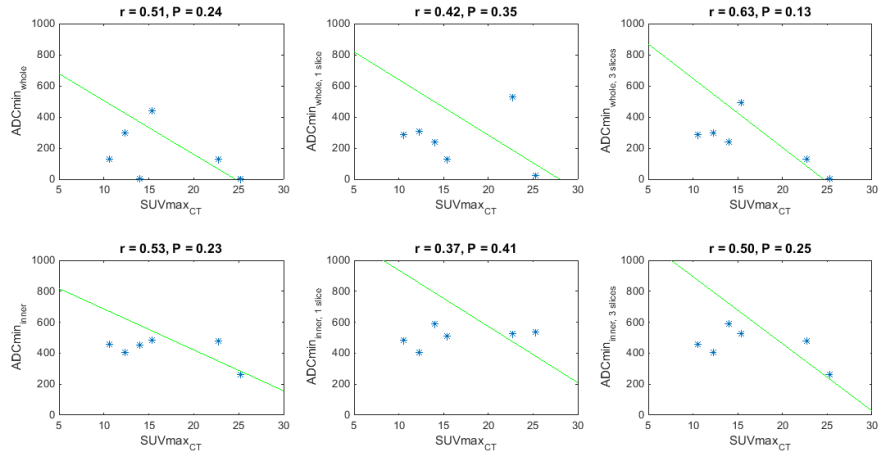

Figure A.7: No correlation was found between ADCmin and $\text{SUVmax}_{\text{CT}}$ in any of the six different shaped ROIs.

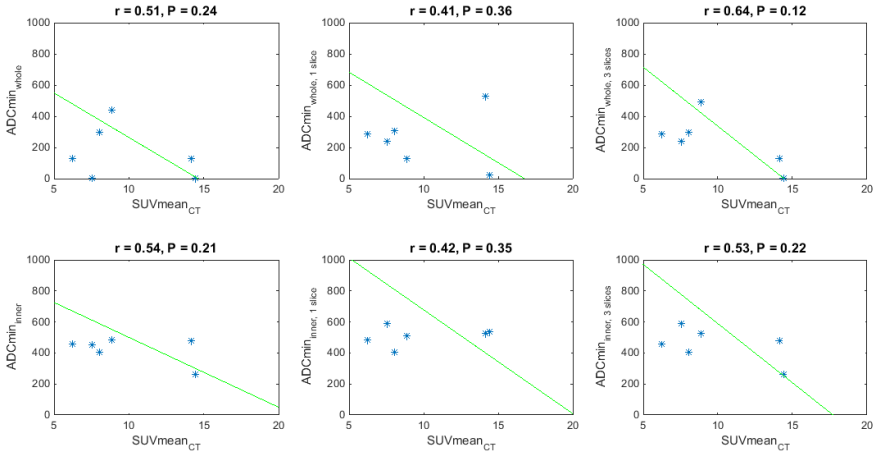

Figure A.8: No correlation was found between ADCmin and $\text{SUVmean}_{\text{CT}}$ in any of the six different shaped ROIs.

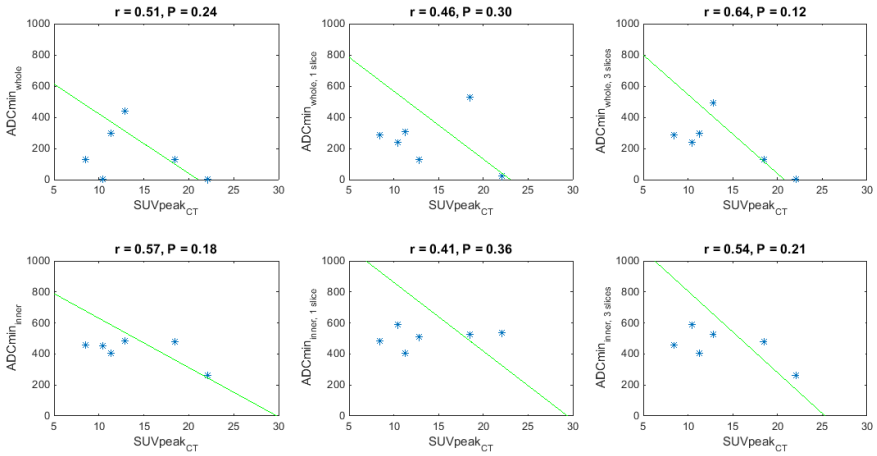

Figure A.9: No correlation was found between ADCmin and $\text{SUVpeak}_{\text{CT}}$ in any of the six different shaped ROIs.

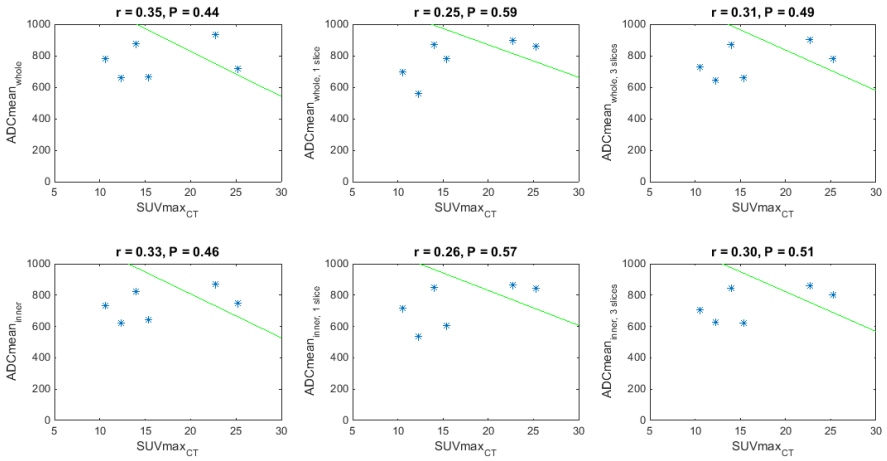

Figure A.10: No correlation was found between ADCmean and $\text{SUVmax}_{\text{CT}}$ in any of the six different shaped ROIs.

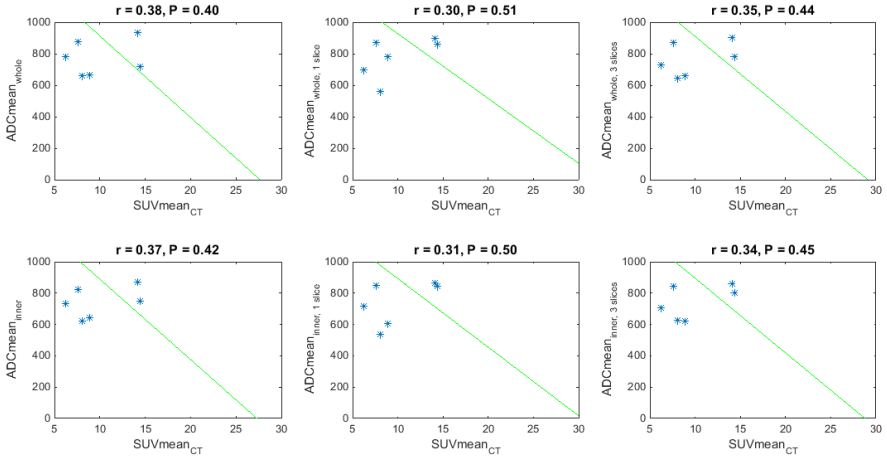

Figure A.11: No correlation was found between ADCmean and $\text{SUVmean}_{\text{CT}}$ in any of the six different shaped ROIs.

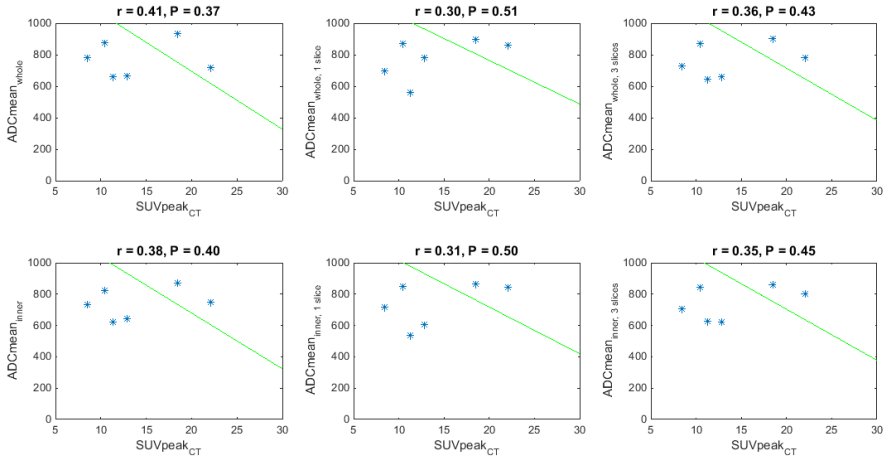

Figure A.12: No correlation was found between ADCmean and $\text{SUVpeak}_{\text{CT}}$ in any of the six different shaped ROIs.